Research Square

Preprints are preliminary reports that have not undergone peer review.
They should not be considered conclusive, used to inform clinical practice,
or referenced by the media as validated information.

Learning in Continuous Action Space for Determination of High Dimensional Potential Energy Surfaces

Subramanian Sankaranarayanan (ssankaranarayanan@anl.gov)
Argonne National Laboratory
Sukriti Manna
Argonne National Laboratory
Troy Loeffler
Argonne National Lab
Rohit Batra
Argonne National Laboratory
Suvo Banik
Argonne National Laboratory
Henry Chan
Argonne National Laboratory https://orcid.org/0000-0002-8198-7737
Kiran Sasikumar
Avant-Garde Materials Simulation
Michael Sternberg
Argonne National Laboratory
Tom Peterka
Argonne National Laboratory
Mathew Cherukara
Argonne National Lab https://orcid.org/0000-0002-1475-6998
Stephen Gray
Argonne National Laboratory
Bobby Sumpter
Oak Ridge National Laboratory https://orcid.org/0000-0001-6341-0355

Physical Sciences - Article

Keywords: Reinforcement learning (RL), potential energy surfaces (PES), inter- and intra-molecular interactions, latent space

Posted Date: March 13th, 2021

DOI: https://doi.org/10.21203/rs.3.rs-284625/v1

License: This work is licensed under a Creative Commons Attribution 4.0 International License.
Read Full License

Learning in Continuous Action Space for Determination of High Dimensional Potential Energy Surfaces

Sukriti Manna[1,2], Troy D. Loeffler[1], Rohit Batra[1], Suvo Banik[1,2], Henry Chan[1], Kiran Sasikumar[1], Michael Sternberg[1], Tom Peterka[5], Mathew J Cherukara[4], Stephen K. Gray[1], Bobby G. Sumpter[3], and Subramanian Sankaranarayanan[1,2]

[1]Center for Nanoscale Materials, Argonne National Laboratory, Lemont, Illinois 60439, United States

[2]Department of Mechanical and Industrial Engineering, University of Illinois, Chicago, Illinois 60607, United States

[3]Center for Nanophase Materials Sciences, Oak Ridge National Laboratory, Oak Ridge, Tennessee 37831, United States

[4]Advanced Photon Source, Argonne National Laboratory, Lemont, Illinois 60439, United States

[5]Math and Computer Science Division, Argonne National Laboratory, Lemont, Illinois 60439, United States

February 27, 2021

Abstract

Reinforcement learning (RL) approaches that combine a tree search with deep learning have found remarkable success in searching exorbitantly large, albeit discrete action spaces, as demonstrated recently in board games like chess, Shogi and Go. Many real-world materials discovery and design applications, however, involve multi-dimensional search problems and learning domains that have continuous action spaces. Exploring high-dimensional potential energy surfaces (PES) of materials to represent inter- and intra-molecular interactions, for example, involves a continuous action search to find optimal potential parameters or coefficients. Traditionally, these searches are time consuming (often several years for a single system) and have been driven by human intuition and/or expertise and more recently by global/local optimization searches that have issues with convergence and/or do not scale well with the search dimensionality. Here, in a departure from discrete action and other gradient-based approaches, we introduce a RL strategy based on decision trees that incorporates modified rewards for improved exploration, efficient sampling during playouts and a "window scaling scheme" for enhanced exploitation, to enable efficient and scalable search for continuous action space problems. Using high-dimensional artificial landscapes and control RL problems, we successfully benchmark our approach against popular global optimization schemes and state of the art policy gradient methods, respectively. We further demonstrate its efficacy to perform high-throughput PES search for 54 different elemental systems across the Periodic table, including alkali, alkaline-earth, transition metals, metalloids, as well as non-metals. Using a well-sampled ($\sim$165,000 configurations) first-principles derived training and test dataset, we demonstrate that the new class of RL trained bond-order potentials capture the size-dependent energetic landscape from few atom clusters to bulk (energy errors $<<$ 200 meV/atom over a 3-6 eV sampled range) as well as their dynamics (force errors $<<$ 0.5 eV/Å over a 50-100 eV/Å range). We analyze the error trends across different elements in the latent space and trace their origin to elemental structural diversity and the smoothness of the element energy surface. Finally, we run molecular dynamics using these RL trained potentials and perform a comprehensive test of dynamic stability of more than 40,000 clusters sampled for different elements across the Periodic table. Our newly developed high-quality potentials will enable accelerated nanoscale materials design and discovery. Broadly, our RL strategy will be applicable to many other physical science problems involving search over continuous action spaces.

Reinforcement learning (RL) and decision tree (e.g., Monte Carlo tree search) based RL algorithms are emerging as powerful machine learning approaches, allowing a model to directly interact with and learn from the environment [1]. RL has achieved impressive capabilities with tremendous success in solving problems with intractable search space, for example in game playing (such as chess, Shigo, and Go) [2, 3], chemical synthesis planning [4, 5] or drug discovery [6]. However, these methods have been limited to discrete action space—e.g., "move pawn to e4", "add acetone reagent" or "remove chemical group -COOH" [7]. Many real-world problems including several grand challenges in materials discovery and design involve decision making and search *via* continuous action space [8]. These include, for instance, the problem of searching optimal model parameters/weights, exploring low energy material phases or inverse design, optimizing experimental parameters or synthesized material properties [5, 9]. While it is highly desirable to translate the merits of RL methods to solve search problems in materials design, a challenge lies in its continuous, complex and multi-dimensional nature and is further complicated by an exorbitantly large number of degenerate and/or sub-optimal solutions.

One of the more successful versions of RL involves use of Monte Carlo tree search (MCTS) [10], which utilizes playouts to select the best possible action (with maximum reward) from the current state (Figure 1). Here, playouts refer to random actions from the model that allow it to learn by interacting with the environment. The larger the number of playouts, the better the model estimate of reward, and the more promising is the model action selection. Notably, the MCTS performs this search in a tree-structure, continuously growing either those leafs of the tree that result in maximum reward (exploitation) or those which have not been adequately sampled (exploration)[11]. It is important to understand that when the action space is discrete, a parent leaf will exhibit limited possible child leaves, all (or some) of which can be assessed for their prominence. When the action space is continuous, the number of possible child leaves are infinite, irrespective of the depth of the parent leaf, making the use of MCTS seemingly impossible in a continuous action space.

In a significant departure from traditional MCTS approaches [12], we introduce three concepts to tackle continuous action space problems: (1) a uniqueness function to avoid degeneracy, (2) correlating tree depth to action space, and (3) implementing an adaptive sampling of playouts. The first ensures that only unique leaves are being explored during MCTS. This avoids the common issue of convergence of two initially separate MCTS branches to the same region of the continuous search space. More importantly, this resolves the problem of multiple representations of the same (degenerate) solution as often encountered in several physical problems (for example, a phase structure can be represented using varying unit cell definitions). The second concept provides a meaningful structure to the algorithm, with the child leaf searching within a narrower region of that of the parent node. Lastly, to improve the quality of the playouts, especially in the case of high dimensional search space, the random simulations were biased to sample those regions that were closer to the parent leaf.

We deploy our approach to a representative high-dimensional and continuous parameter search that involves navigating through high-dimensional potential energy surfaces [13] of elemental nanoclusters and bulk systems. Historically, this has represented a major challenge for molecular modeling and has been accomplished using human intuition and expertise, requiring years of painstaking efforts. Recently, a variety of global/local optimization methods have emerged for this task [14, 15], but they either have convergence issues, do not scale well with the search dimensionality, or cannot incorporate important gradient-free knowledge (e.g., dynamic stability). Over several decades, these approaches have been used to develop a large number of multi-parameter physics-based models, mainly for bulk systems and their static/dynamical properties. Their extrapolation to capture nanoscale properties and dynamics, however, shows strong deviation from the ground truth (estimated using high-fidelity first-principles models, such as density functional theory). Here, we demonstrate the efficacy of our continuous action MCTS (c-MCTS) by developing a hybrid bond-order potential (an 18 dimensional parameter space) for 54 elements chosen across the Periodic table, capturing a variety of bonding environments and demonstrating the generality, efficiency and robustness of our approach. For each element, we train by fitting energies of thousands of carefully sampled (see Methods) nanoclusters of varying sizes, which are particularly known for their complex chemistry[16, 17] and are difficult to train using traditional optimization strategies. Our ML trained bond-order potentials show significant performance improvement over current physics-based potential models in terms of energies, atomic forces and dynamic stability, and generalize well for dynamical properties that were not included during model training.

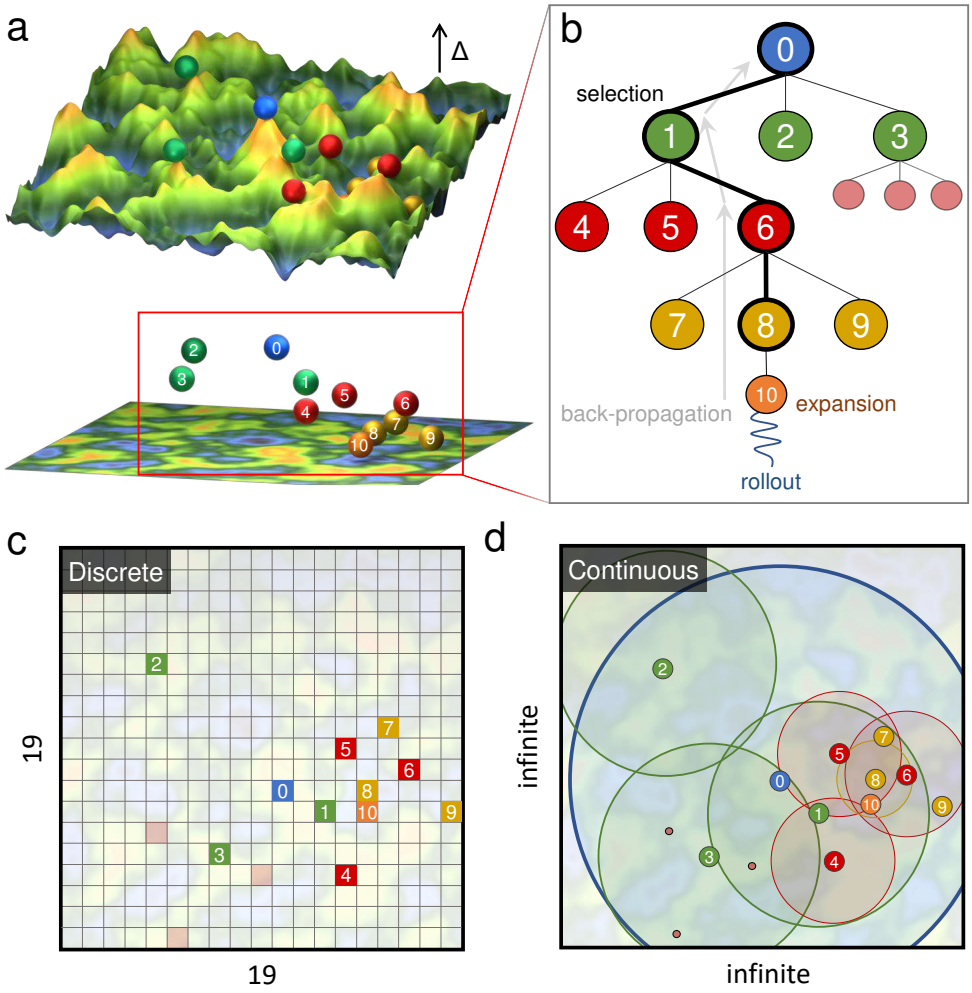

Figure 1: **Schematic of the continuous action MCTS algorithm applied for exploration of high-dimensional potential energy surfaces** a) Top: Simplistic representation of an objective landscape for a 2-parameter search problem. In-plane axes corresponds to (two) independent model parameters. Out-of-plane axis corresponds to objective values, which is defined as the weighted sum of the error in model predicted energies of clusters with respect to target energies. This objective is minimized by our c-MCTS algorithm. The spheres represent candidates of different model parameters within a MCTS run, where differences in their vertical positions indicate differences in their objective values. Bottom: Slightly tilted view of the above with the surface represented as a contour map below the spheres. The numbering on the spheres corresponds to their node positions in the MCTS tree shown in (b). These numbers roughly correspond to the order that the candidates are explored. b) Schematic showing the root, parent, child nodes and their relationship within a MCTS tree structure. A typical MCTS search involves node selection, expansion, simulation (playout), and back-propagation. Different coloring of the nodes indicates different depth in the MCTS tree. The algorithm balances between exploration (lateral expansion of nodes) and exploitation (depth expansion of nodes). As shown in (a), the objective value of a MCTS run is expected to decrease quickly along the depth of the tree. c) Search space of a traditional MCTS algorithm, *e.g.*, game board, is discrete. In the context of parameter optimization, for two discrete parameters each of 19 possible values, the search space consists of a finite 361 search positions. d) The problem of parameter search, such as the objective surface illustrated in (a), generally involves parameters that are continuous, which corresponds to infinite possible search positions. We handle this challenge by applying a range-funneling technique to the MCTS algorithm where the search neighborhood at each tree depth becomes smaller and smaller such that the algorithm can converges to the optimal solutions.

Learning in Continuous Action Space

MCTS is a powerful algorithm for planning, optimization and learning tasks owing to its generality, simplicity, low computational requirements, and a theoretical bound on exploration-vs-exploitation trade-off [18, 10, 12]. As illustrated in Figure 1b, it utilizes a tree-structure for the parameter search consisting of four key stages: (1) selection: based on a *tree policy* select the leaf node that has the highest current score; (2) expansion: add a child node to the selected leaf after taking a possible (unexplored) action; (3) simulation: from the selected node, perform Monte Carlo trials of possible actions using a *playout policy* to estimate the associated expected reward; (4) back-propagation: pass the rewards generated by the simulated episodes to update the scores of all the parent leafs encountered while moving up the tree. A popular tree policy to use is the upper confidence bound for parameters (UCP) [19]:

$$\mathrm{UCP}(\theta_j) = -\min(r_1, r_2, ..., r_{n_i}) + c \cdot f(\theta_j) \cdot \sqrt{\frac{lnN_i}{n_i}} \tag{1}$$

where θ_j represents the node j in the MCTS structure, r denotes the reward for a given playout, $c(>0)$ is the exploration constant, n_i is the number of playout samples taken by node θ_j and all of its child nodes, and N_i is the same value as n_i except for the parent node of θ_j. ($f(\theta_j)$ is the uniqueness function specifically introduced in this work and is equal to 1 in traditional MCTS settings.) This policy tries to balance the search between those nodes which have either returned the maximum reward (left term) or have not been explored enough (right term). In contrast, the playout policy selects random actions (from a node) until the simulated episode is over.

Several issues deter the use of the traditional MCTS formulation for continuous action space. First, from any parent node, the number of possible child nodes is infinite as the action space is continuous. Further, for problems involving parameter search or optimization, the same set of actions are possible irrespective of the current depth of the tree, thus, rendering the tree-structure meaningless. Second, the search space of several physical problems display inherent symmetries, which are not properly accounted for in the traditional MCTS. This leads to poor search efficiency, especially in high-dimensional problems, or sometimes unwanted convergence of different MCTS branches to the same solution. Lastly, performing random actions during the playout policy may be useful to learn expected returns for game playing, but do not translate well in high-dimensional continuous action space due to the well-known "curse of dimensionality" [20] (see Supplementary Information Section 1).

We introduce three concepts to enable MCTS operations for continuous actions space, namely, the uniqueness function, a tree-depth based adaptive action space, and a dimensionality-dependent playout policy. First, the uniqueness function $f(\theta_j)$ for a node θ_j returns a value between 0 and 1, with a higher value indicating the uniqueness of this node with respect to all the other nodes in the tree. This not only helps avoid degenerate actions, but also promotes explorations of those actions that are dissimilar to the previous ones, thereby efficiently sampling a larger search region. This is among the most essential feature of c-MCTS that enables high search efficiency. The definition of $f(\theta_j)$ used in this work (see Section 1.1 in Supplementary Information) and its performance for high-dimensional continuous space is demonstrated in Extended Figure 1 and Table 1.

Second, an adaptive action space that depends on the tree-depth was included to provide better child-parent correlation within the MCTS tree-structure. As illustrated in Figure 1d, in this new scheme the range of possible actions from a node continually decreases as we go down the tree-depth. This ensures that the child node is based on actions that are within the search scope of its parent node. Further, this allows the MCTS algorithm to incrementally refine its search space; larger scans are made in the initial phase of the search, followed by more focused search in the identified interesting regions. This also restores a meaningful correlation between the parent and the child node, and allows the algorithm to converge to a reasonable optimal solution as one moves down the tree. More details on the appropriate choice of the window scaling parameter with tree depth is provided in Supplementary Information Section 1.

Third, we introduce an efficient MCTS playout policy for high-dimensional continuous action space. Traditional MCTS relies on playout policy with random moves, but when the search space is intractable such a policy can make the learning process extremely difficult and inefficient. [21, 22]. For example, even with the tree-depth based scaling of action space, a random playout (assuming uniform probability distribution) will have a high change of action selection which is far from the parent node; see Supplementary Information

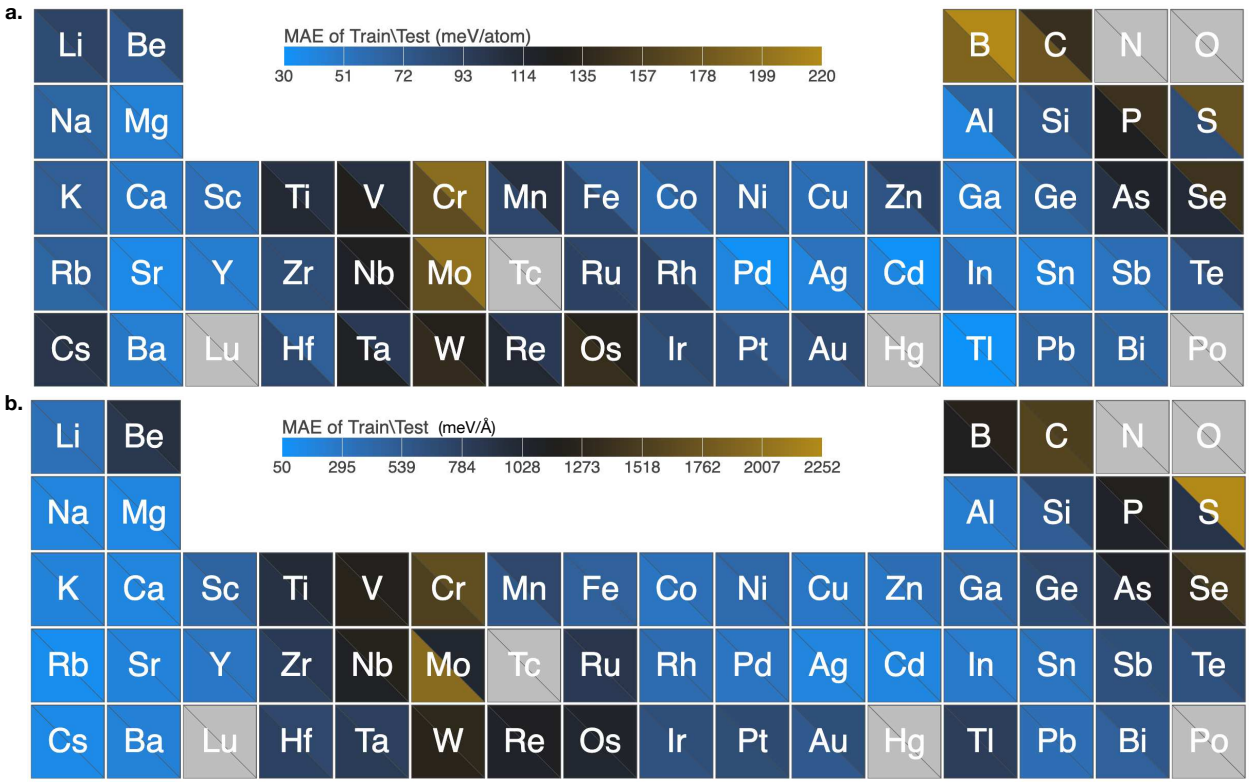

Figure 2: **HyBOP model performance after high-throughput exploration of the potential energy surface of nanoclusters using continuous action MCTS.** A bond order model with Tersoff-type formalism for 54 different elements across the Periodic table is parameterized using an extensive training dataset generated from density functional theory (DFT) computations. The training set includes nanoclusters of varying sizes and shapes (∼1500 configurations and their energies) for each of the different elements. Mean absolute error (MAE) in (a) energy and (b) force predictions of the bond order force-fields relative to the reference DFT model on a test set of ∼70,000 configurations is shown using the color bar in meV/atom and meV/Å units, respectively.

(section 1.2) for a discussion on how uniform or multivariate Gaussian probability distribution based playout policies systematically select actions that have large displacements from the parent node. To avoid this issue, we used a biased playout policy that selects action based on the probability distribution $\boldsymbol{r}^{-(d-1)}$ where $\boldsymbol{r}$ is the distance from the parent node, and d is the dimensionality of the search space. Based on our experiments, we found this playout policy to provide significant improvement in the performance owing to better action selections.

We first demonstrate the efficacy of our approach by comparing its performance with other state-of-the-art evolutionary and gradient-based approaches [23] on 25 well-known trial functions or artificial landscapes, containing deceitful local minima and a high-dimensional search space, (see Extended Figure 1 and Table 1 and Supplementary Information (Section 2.1). Our c-MCTS algorithm outperforms other approaches both in terms of the solution quality (maximum reward) and search efficiency (low computational cost). Especially for trial functions with higher dimensionality (e.g., > 50), we note that the performance of c-MCTS is clearly superior to other representative and popular optimizers, illustrating the appeal of c-MCTS for multi-dimensional materials design and discovery problems. We also applied c-MCTS to classic reinforcement problems with a continuous action space. As shown in Supporting Information Figure S6, c-MCTS performs on par with state-of-the-art policy gradient methods.

High-throughput Navigation of High-dimensional PES

As a representative impactful materials application, we next demonstrate the ability of our c-MCTS approach to successfully navigate through an 18-dimensional potential energy landscape (see Methods section and Supporting Information for a description of the hybrid bond-order formalism) for 54 different elements that include alkali element, alkaline-earth elements, transition element, rare-earth, metalloids and non-metals. We assess the performance of the optimized hybrid bond-order potentials (HyBOP) [24] with respect to the ground truth, i.e., density functional theory (DFT) computed energies and forces of ∼165,000 total configurations (including both low-energy near equilibrium (0.5-1.5 eV range) and high-energy non-equilibrium configurations (1.0-8.0 eV range) in our training (∼95,000) and test (∼70,000) datasets. As shown in Figures 2a and b, ML optimized HyBOP displays remarkable performance for all the elements across the Periodic table. MAE in cluster energies of Group IV-IB transition metals is ∼90 meV/atom and ∼88 meV/atom for the training and test set, respectively. Corresponding values for the post-transition metals from Group IIB (e.g. Zn, Cd) are slightly smaller at ∼60 meV/atom and ∼90 meV/atom, while elements in Group IVA (e.g. Pb) and Group VA (e.g. Bi) display MAE of ∼65 meV/atom for both the training and test. Non-metals that include C, P, S and Se show relatively higher average MAE of ∼138 meV/atom on the training and test datasets, while metalloids such as, B, Si, Ge, As, Sb and Te, have an average MAE of ∼100 meV/atom. Group IA alkali elements, including Li, Na, K, Rb and Cs, have an average MAE of ∼77 meV/atom on both the training and test datasets. Similarly, Group IIA elements from Be to Ba show an average MAE of ∼51 meV/atom. Note that the MAE, as expected, are slightly higher for highly non-equilibrium clusters compared to the near-equilibrium configurations. Overall, our newly trained HyBOP models display remarkable performance in capturing vast regions of the energy landscape, with energies sampled from near-equilibrium to highly non-equilibrium cluster configurations and with sizes from dimers to bulk like cluster configurations (>50 atoms).

We next assess the performance of our c-MCTS trained HyBOP models by comparing the forces experienced by atoms for the various sampled configurations with that computed from DFT. Note that forces were not included in the training. The high-quality of our c-MCTS trained HyBOP models is evident from the strong correlation across a large number of non-equilibrium nanoclusters (total ∼145,000 that have a wide range ∼100 eV/Å for forces) in our test data set (see supporting information). As seen in Figure 2b, the trend in MAE prediction errors on forces is similar to that seen in energies. The Group IA alkali and Group IIA alkali earth metals such as Li, Na, K, Rb, Cs, Mg, Ca, Sr and Ba have force MAE of ∼187 meV/Å. Transition metals as Cu, Ag, Au, Pd have marginally higher MAE ∼300 meV/Å compared to the alkali and alkali earth elements. Magnetic elements such as Fe, Co, Mn, Ni from transition block element have a MAE ∼450 meV/Å in force prediction. Metalloids (B, Si, Ge, As, Sb, Te) from Group IIIA and Group VIA, respectively have a MAE ∼800 meV/Å in force prediction (and MAE ∼99 meV/atom in energy prediction). The block of transition metal elements containing 25 different elements with d electrons have average MAE ∼720 meV/atom in force predictions (MAE ∼90 meV/atom in energies). Non-metals such as C, B, P, S from Group IVA and Group VA display a strong correlation with DFT forces over a wide range (∼200 eV/Å) but have a relatively higher MAE prediction error of 1300 meV/Å compared to the rest.

Notably, we find both the energy and force predictions of c-MCTS optimized HyBOP models to be significantly better than many other commonly available potential models for several of these elements. While not exhaustive, we compare the model performance for 38 different elements covering a range of existing potential types [25], such as EAM, MEAM, Tersoff, AIREBO, ADP and SW, in the Supporting Information. In comparison to the heat map shown in Figure 2, Extended Figure 2 depicts the corresponding MAE generated from some of these best performing force fields available in literature. We note that the errors in energies and forces predicted by the best existing potential are >> 220 meV/atom and >> 2252 meV/Å, respectively for the different elements shown in Extended Figure 2. This is much higher than those for our ML trained models (see Figure 2). This dramatic improvement in the performance can be attributed to two factors, first, the complex chemistry of the nanoclusters that is distinct from bulk-like behavior to which the existing potentials are primarily fit to, and second, the ability of the c-MCTS to find accurate fitting parameters as compared to human intuition. Further details on the MAE obtained for different systems using existing potentials are provided in the Supplementary Information Section 5. In addition to the energies and forces, we also evaluate bulk properties (lattice constants, cohesive energies and elastic constants) predicted by our HyBOP model for ∼ 150 different polymorphs of these 54 elements. We note that the inclusion of

larger bulk-like cluster configurations (> 50 atom clusters) in the training set and longer range interactions in HyBOP ensured that bulk properties are reasonably captured by our models (see Extended Table 3-5 and Extended Figure 3 - 4).

Trends in Elemental Errors and Their Origins

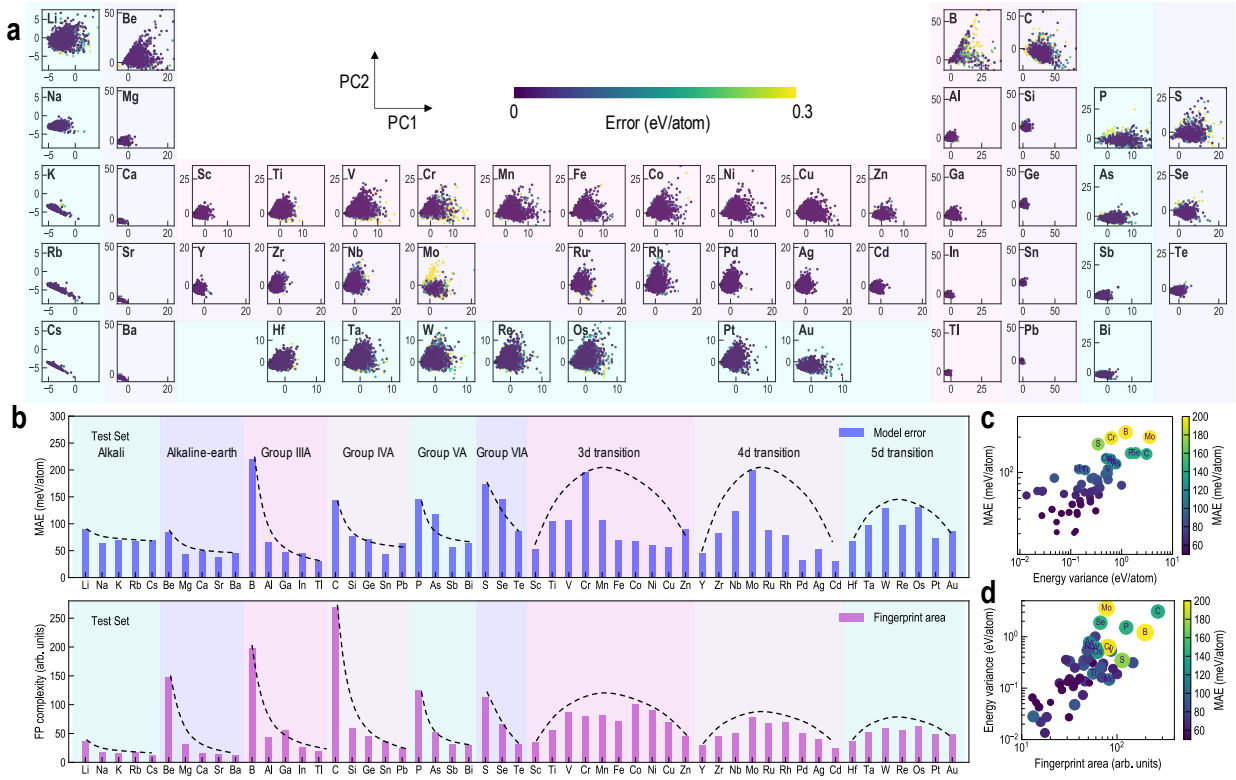

Figure 3: **Trends in model prediction errors with structural diversity of the element.** (a) SOAP fingerprint representation of clusters across different elements as projected along the first two principal components (PCs). The area covered by an element in the PC space is proportional to its structural diversity, and thus, the difficulty to train an accurate potential model. Also, the structural diversity of an element is closely related to its position in the Periodic table. Regions of higher errors mostly occur at the boundary of the PC space which are expected to belong to under-represented configurations. (b) Trend in the prediction errors for different elements when grouped across different columns or rows of the Periodic Table. A similar trend can be seen for the elemental PC area, suggesting that elemental structural diversity correlates well with the model errors. The dotted lines capture the approximate trend within a group of elements and guide the eye. (c) Correlation between the prediction error and the inverse of the smoothness of the element energy surface. (d) Elements with high prediction errors display either high structural diversity or exhibit highly corrugated energy surface. Elements with mean absolute error (MAE) >100 meV/atom have been marked in (c) and (d).

We next aim to understand the relationship between the chemistry and the HyBOP model performance for any underlying element. We project the complete cluster test dataset in a 2D principal component (PC) space as shown in Figure 3a. A popular fingerprinting scheme, SOAP or smooth overlap of atomic positions [26], that transforms structural arrangement of a cluster to a unique vector representation was utilized (see Methods). A larger span in the PC space by an element is characteristic of its higher structural diversity; for example, some of the well-known elements with most diverse chemical bonding, such as B, C and S, can be seen to have a much larger PC span. We find a strong correlation of this PC area with the element position

in the Periodic table; moving down the columns of alkali, alkaline-earth, Group IIIA, Group IVA, Group VA and Group VIA elements, we note that the configurational diversity systematically decreases. Similarly, moving across the 3d, 4d and 5d transition rows, the spanned PC area first increases and then decreases in accordance with the number of valence d-electrons. A good match between the expected chemical diversity and the spanned PC area of an element is indicative of a well sampled and comprehensive (training and test) cluster dataset. Another notable aspect from Figure 3a is that many of the clusters with high prediction errors lie at the boundary of the PC space which are expected to belong to under-represented regions of the potential energy surface. An improvement in the model performance is thus expected if more clusters from such regions are included in the training dataset. When grouped according to the position in the Periodic

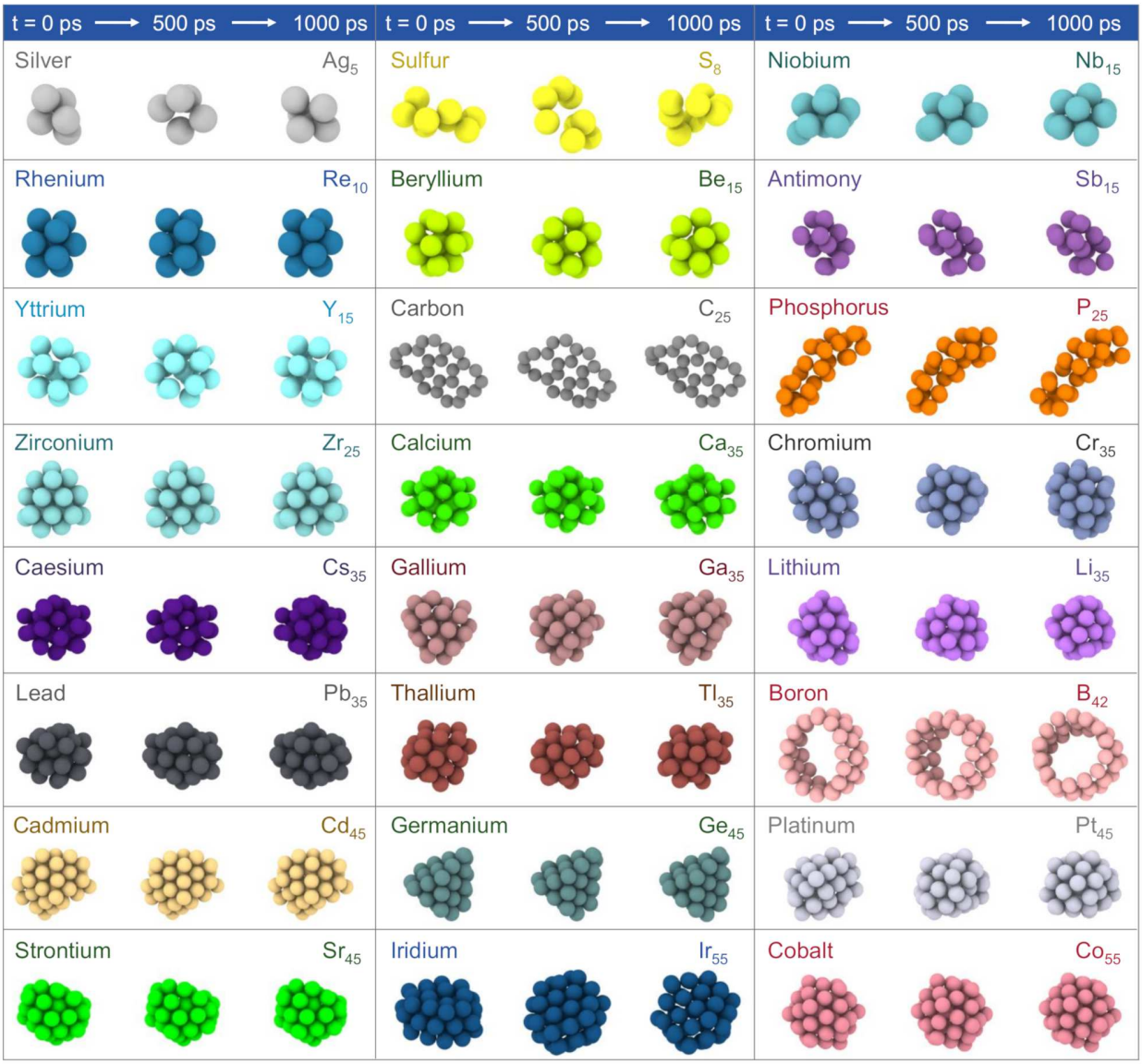

Figure 4: **Dynamic stability of the clusters of various representative elemental systems.** Snapshots sampled from 1 nanosecond MD simulation trajectories illustrate the dynamic stability of the clusters of representative topologies and sizes for the different elements. To rigorously test the dynamic stability, MD simulations were performed for $>$ 40,000 nanoclusters for the 54 different elements in different size ranges. More detailed MD trajectories for each element and the simulated temperatures are included in the Supplemental Information Section 10.

table, the errors in the model energy prediction roughly evolve as per the element chemistry (see Figure 3b). Moving down the columns of alkali, alkaline-earth, Group IIIA, Group IVA, Group VA and Group VIA elements the model prediction errors systematically decrease (within certain approximation), while moving across the 3d, 4d and 5d transition rows, such errors first increase and then decrease. These trends are consistent with the above discussion on configurational diversity, as captured by the spanned PC area. To further quantify this correlation, the area in the 2D PC space was computed using a convex hull construction, and can be seen to match well with the errors in model predictions (Figure 3b)—with the notable exception of Mo, which had a relatively high model error than expected from the respective configurational diversity value. We argue that developing potentials for elements that show large configurational diversity, or large PC area, should be more difficult. This is because finding a unique set of the HyBOP parameters that capture all such high energy regions of the energy surface is non-trivial.

Another aspect that can make potential learning more difficult is the smoothness of the energy surface. This implies that small perturbations in an element's configuration leads to energy changes with high variance. Developing a potential for such a system would be difficult as the underlying energy surface would be highly corrugated with strong variations in energy depending on the direction of the perturbation, or could contain multiple local minima. Based on the principle of a variogram [27], the variance in energy changes for an element was computed by measuring the corresponding SOAP fingerprint distances between different, but similar, configurations. As shown in Figure 3c, elements with large prediction errors also displayed high variance in the energy changes, and vice versa. Combining both the above aspects in Figure 3d, it can be seen that models with high prediction errors belong to cases with either high structural diversity or highly corrugated energy surface; almost all elements with MAE >100 meV/atom lie in the upper right corner of Figure 3d. Therefore, this analysis not only explains the observed trends in the model prediction errors across the Periodic table, but also provides confidence that the developed c-MCTS search successfully found highly optimal HyBOP parameters in all cases.

Dynamic Stability of Clusters to bulk

Finally, we perform a rigorous test of our c-MCTS-optimized HyBOP potentials by evaluating the dynamic stability of the 54 elemental nanoclusters with different topologies and over a broad size range (5 to 50 atoms) at different temperatures. We perform MD simulations and analyze the dynamical stability for most clusters using the mean square deviation (MSD) of the atoms during a 1 ns trajectory. A cluster is considered to be dynamically unstable if the MSD is greater than 2 Å; for a few special configurations, such as rings, visual inspection of energy or configuration trajectory was used to evaluate dynamical stability as system rotations lead to artificially higher values of MSD. We find that the c-MCTS optimized models capture the dynamical stability across > 40,000 clusters tested, with a few representative trajectories shown in Figure 4. Detailed trajectories for each element are included in the Supporting Information. This rigorous validation provides confidence for the future use of the developed potential models as well as the c-MCTS framework for exploring various structural and dynamical properties of nanoscale systems.

In summary, we build on the powerful ideas of reinforcement learning and decision trees to develop an effective search algorithm in high-dimensional continuous action space (c-MCTS). Our algorithm extends Monte Carlo tree search to continuous action spaces with three novel concepts (uniqueness criteria, window scaling and adaptive sampling) to accelerate the search. c-MCTS broadly outperforms state-of-the-art meta-heuristic and other optimization methods. We applied this method to develop accurate bond-order potentials (with 18 dimensional search space) for 54 elements across the Periodic table, a rather non-trivial feat which would have taken years of efforts with the traditional approach. On the one hand, the developed potentials will be of use to the materials simulation community owing to their accuracy in capturing energy and atomic forces across large configuration space, making them attractive in the field of catalysis, especially for problems involving single-atom-catalysts [28, 29]that form localized active sites. On the other hand, the developed c-MCTS will be beneficial in solving grand challenges in materials discovery that often involve search in a continuous space.

Acknowledgements

This material is based upon work supported by the U.S. Department of Energy, Office of Science, Office of Basic Energy Sciences Data, Artificial Intelligence and Machine Learning at DOE Scientific User Facilities program under Award Number 34532. This work was performed in part at the Center for Nanoscale Materials, the Advanced Photon Source and the Center for Nanophase Materials Sciences, which are US Department of Energy Office of Science User facilities supported by the U.S. Department of Energy, Office of Science, Office of Basic Energy Sciences, under Contract No.s DE-AC02-06CH11357, DE-AC02-06CH11357 and DE-AC05-00OR22725, respectively. This research used resources of the National Energy Research Scientific Computing Center, which was supported by the Office of Science of the U.S. Department of Energy under Contract No. DE-AC02-05CH11231. An award of computer time was provided by the Innovative and Novel Computational Impact on Theory and Experiment (INCITE) program of the Argonne Leadership Computing Facility at the Argonne National Laboratory, which was supported by the Office of Science of the U.S. Department of Energy under Contract No. DE-AC02-06CH11357. The authors would also like to acknowledge the support from the UIC faculty start-up fund. This research used resources of the National Energy Research Scientific Computing Center (NERSC), a U.S. Department of Energy Office of Science User Facility located at Lawrence Berkeley National Laboratory, operated under Contract No. DE-AC02-05CH11231. The authors thank Dr. Badri Narayanan for useful discussions.

Code Availability

The c-MCTS algorithm is implemented in the BLAST framework developed by the authors. The codes, scripts and the framework are available from the authors upon reasonable request.

Data Availability

The data that support the findings of this study are available from the authors upon reasonable request.

Author Contribution

SM, RB and SKRS conceived and designed the project. TDL, and RB contributed equally. TDL developed the RL framework for continuous action space problems with input from SM, HC and SKRS. TDL evaluated the performance of the high-dimensional trial functions. SM deployed the RL c-MCTS algorithm and trained the bond order potential functions for the various elements across the periodic Table. All the first-principles datasets were generated by SM. Validation of the force-fields were carried out by SM and SB. RB developed an ML framework to carry out the analysis of the error trends in the potential functions across the different elemental systems. SB performed the high-throughput simulations to evaluate the dynamical stability of all the different elemental clusters. HC integrated the c-MCTS algorithm into the BLAST multi-fidelity framework. TDL carried out validation of the c-MCTS on training high-dimensional neural networks. All the authors contributed to the data analysis and to the preparation of the manuscript. SM, RB and SKRS wrote the manuscript with input from all the co-authors. SKRS supervised and directed the overall project.

References

[1] Richard S Sutton and Andrew G Barto. *Reinforcement learning: An introduction*. MIT press, 2018.

[2] David Silver, Aja Huang, Chris J Maddison, Arthur Guez, Laurent Sifre, George Van Den Driessche, Julian Schrittwieser, Ioannis Antonoglou, Veda Panneershelvam, Marc Lanctot, et al. Mastering the game of go with deep neural networks and tree search. *Nature*, 529(7587):484–489, 2016.

[3] David Silver, Thomas Hubert, Julian Schrittwieser, Ioannis Antonoglou, Matthew Lai, Arthur Guez, Marc Lanctot, Laurent Sifre, Dharshan Kumaran, Thore Graepel, et al. A general reinforcement learning algorithm that masters chess, shogi, and go through self-play. *Science*, 362(6419):1140–1144, 2018.

[4] Xiaoxue Wang, Yujie Qian, Hanyu Gao, Connor W Coley, Yiming Mo, Regina Barzilay, and Klavs F Jensen. Towards efficient discovery of green synthetic pathways with monte carlo tree search and reinforcement learning. *Chemical Science*, 11(40):10959–10972, 2020.

[5] Rohit Batra, Le Song, and Rampi Ramprasad. Emerging materials intelligence ecosystems propelled by machine learning. *Nature Reviews Materials*, pages 1–24, 2020.

[6] Mariya Popova, Olexandr Isayev, and Alexander Tropsha. Deep reinforcement learning for de novo drug design. *Science Advances*, 4(7):eaap7885, 2018.

[7] Kyunghoon Lee, Jin Woo Kim, and Woo Youn Kim. Efficient construction of a chemical reaction network guided by a monte carlo tree search. *ChemSystemsChem*, 2000.

[8] Gabriel Dulac-Arnold, Richard Evans, Hado van Hasselt, Peter Sunehag, Timothy Lillicrap, Jonathan Hunt, Timothy Mann, Theophane Weber, Thomas Degris, and Ben Coppin. Deep reinforcement learning in large discrete action spaces. *arXiv preprint arXiv:1512.07679*, 2015.

[9] Keith T Butler, Daniel W Davies, Hugh Cartwright, Olexandr Isayev, and Aron Walsh. Machine learning for molecular and materials science. *Nature*, 559(7715):547–555, 2018.

[10] Levente Kocsis and Csaba Szepesvári. Bandit based monte-carlo planning. In *15th European conference on machine learning*, pages 282–293. Springer, 2006.

[11] Guillaume M JB Chaslot, Mark HM Winands, H JAAP VAN DEN HERIK, Jos WHM Uiterwijk, and Bruno Bouzy. Progressive strategies for monte-carlo tree search. *New Mathematics and Natural Computation*, 4(03):343–357, 2008.

[12] Cameron B Browne, Edward Powley, Daniel Whitehouse, Simon M Lucas, Peter I Cowling, Philipp Rohlfshagen, Stephen Tavener, Diego Perez, Spyridon Samothrakis, and Simon Colton. A survey of monte carlo tree search methods. *IEEE Transactions on Computational Intelligence and AI in games*, 4(1):1–43, 2012.

[13] David J Wales, Jonathan PK Doye, Mark A Miller, Paul N Mortenson, and Tiffany R Walsh. Energy landscapes: from clusters to biomolecules. *Advances in Chemical Physics*, 115:1–112, 2000.

[14] Henry Chan, Badri Narayanan, Mathew J Cherukara, Fatih G Sen, Kiran Sasikumar, Stephen K Gray, Maria KY Chan, and Subramanian KRS Sankaranarayanan. Machine learning classical interatomic potentials for molecular dynamics from first-principles training data. *The Journal of Physical Chemistry C*, 123(12):6941–6957, 2019.

[15] Rohit Batra and Subramanian Sankaranarayanan. Machine learning for multi-fidelity scale bridging and dynamical simulations of materials. *Journal of Physics: Materials*, 3(3):031002, 2020.

[16] JP Wilcoxon and BL Abrams. Synthesis, structure and properties of metal nanoclusters. *Chemical Society Reviews*, 35(11):1162–1194, 2006.

[17] Indranath Chakraborty and Thalappil Pradeep. Atomically precise clusters of noble metals: emerging link between atoms and nanoparticles. *Chemical reviews*, 117(12):8208–8271, 2017.

[18] Rémi Coulom. Efficient selectivity and backup operators in monte-carlo tree search. In *5th International conference on computers and games*, pages 72–83. Springer, 2006.

[19] Yun-Ching Liu and Yoshimasa Tsuruoka. Modification of improved upper confidence bounds for regulating exploration in monte-carlo tree search. *Theoretical Computer Science*, 644:92–105, 2016.

[20] Bellman Richard E. *Reinforcement learning: An introduction*. Princeton University press, 1957.

[21] Kaushik Subramanian, Jonathan Scholz, Charles L Isbell, and Andrea L Thomaz. Efficient exploration in monte carlo tree search using human action abstractions. In *Proceedings of the 30th International Conference on Neural Information Processing Systems, NIPS*, volume 16, 2016.

[22] Steven James, George Konidaris, and Benjamin Rosman. An analysis of monte carlo tree search. *Proceedings of the AAAI Conference on Artificial Intelligence*, 31(1), Feb. 2017.

[23] Iman Ahmadianfar, Omid Bozorg-Haddad, and Xuefeng Chu. Gradient-based optimizer: A new metaheuristic optimization algorithm. *Information Sciences*, 540:131–159, 2020.

[24] AP Horsfield, AM Bratkovsky, M Fearn, DG Pettifor, and M Aoki. Bond-order potentials: Theory and implementation. *Physical Review B*, 53(19):12694, 1996.

[25] Judith A Harrison, J David Schall, Sabina Maskey, Paul T Mikulski, M Todd Knippenberg, and Brian H Morrow. Review of force fields and intermolecular potentials used in atomistic computational materials research. *Applied Physics Reviews*, 5(3):031104, 2018.

[26] Albert P Bartók, Mike C Payne, Risi Kondor, and Gábor Csányi. Gaussian approximation potentials: The accuracy of quantum mechanics, without the electrons. *Physical Review Letters*, 104(13):136403, 2010.

[27] Mirko Mälicke and Helge David Schneider. Scikit-gstat 0.2. 6: A scipy flavoured geostatistical analysis toolbox written in python. *Disponiblea l'adresse DOI*, 10, 2019.

[28] Xuning Li, Linghui Liu, Xinyi Ren, Jiajian Gao, Yanqiang Huang, and Bin Liu. Microenvironment modulation of single-atom catalysts and their roles in electrochemical energy conversion. *Science Advances*, 6(39):eabb6833, 2020.

[29] Abhaya K Datye and Hua Guo. Single atom catalysis poised to transition from an academic curiosity to an industrially relevant technology. *Nature Communications*, 12(1):1–3, 2021.

[30] The quantum cluster database. http://muellergroup.jhu.edu/quantumclusterdatabase_TEST2/. Accessed: 2020-12-25.

[31] David M Deaven and Kai-Ming Ho. Molecular geometry optimization with a genetic algorithm. *Physical review letters*, 75(2):288, 1995.

[32] Jack BA Davis, Armin Shayeghi, Sarah L Horswell, and Roy L Johnston. The birmingham parallel genetic algorithm and its application to the direct dft global optimisation of ir_n (n= 10-20) clusters. *Nanoscale*, 7(33):14032–14038, 2015.

[33] Troy D. Loeffler, Sukriti Manna, Tarak K. Patra, Henry Chan, Badri Narayanan, and Subramanian Sankaranarayanan. Active learning a neural network model for gold clusters & bulk from sparse first principles training data. *ChemCatChem*, 12(19):4796–4806, 2020.

[34] Frank H Stillinger Jr. Rigorous basis of the frenkel-band theory of association equilibrium. *The Journal of Chemical Physics*, 38(7):1486–1494, 1963.

[35] Steven O Nielsen. Nested sampling in the canonical ensemble: Direct calculation of the partition function from nvt trajectories. *The Journal of chemical physics*, 139(12):124104, 2013.

[36] Georg Kresse and Jürgen Furthmüller. Efficiency of ab-initio total energy calculations for metals and semiconductors using a plane-wave basis set. *Computational materials science*, 6(1):15–50, 1996.

[37] Jean Charles Gilbert and Jorge Nocedal. Global convergence properties of conjugate gradient methods for optimization. *SIAM Journal on optimization*, 2(1):21–42, 1992.

[38] John P Perdew, Kieron Burke, and Matthias Ernzerhof. Generalized gradient approximation made simple. *Physical review letters*, 77(18):3865, 1996.

[39] Henry Chan, Badri Narayanan, Mathew Cherukara, Troy D Loeffler, Michael G Sternberg, Anthony Avarca, and Subramanian KRS Sankaranarayanan. Blast: Bridging length/time scales via atomistic simulation toolkit. *arXiv preprint arXiv:2002.10401*, 2020.

[40] Momin Jamil and Xin-She Yang. A literature survey of benchmark functions for global optimisation problems. *International Journal of Mathematical Modelling and Numerical Optimisation*, 4(2):150–194, 2013.

[41] Lester James Miranda. Pyswarms: a research toolkit for particle swarm optimization in python. *Journal of Open Source Software*, 3(21):433, 2018.

[42] James Bergstra, Brent Komer, Chris Eliasmith, Dan Yamins, and David D Cox. Hyperopt: a python library for model selection and hyperparameter optimization. *Computational Science & Discovery*, 8(1):014008, 2015.

[43] Jerry Tersoff. New empirical approach for the structure and energy of covalent systems. *Physical review B*, 37(12):6991, 1988.

[44] Steve Plimpton. Fast parallel algorithms for short-range molecular dynamics. *Journal of computational physics*, 117(1):1–19, 1995.

[45] Lauri Himanen, Marc OJ Jäger, Eiaki V Morooka, Filippo Federici Canova, Yashasvi S Ranawat, David Z Gao, Patrick Rinke, and Adam S Foster. Dscribe: Library of descriptors for machine learning in materials science. *Computer Physics Communications*, 247:106949, 2020.

[46] Anubhav Jain, Shyue Ping Ong, Geoffroy Hautier, Wei Chen, William Davidson Richards, Stephen Dacek, Shreyas Cholia, Dan Gunter, David Skinner, Gerbrand Ceder, et al. Commentary: The materials project: A materials genome approach to accelerating materials innovation. *Apl Materials*, 1(1):011002, 2013.

Methods

Generation of Diverse Cluster Configurations

The accuracy and transferability of a potential model or force field depends on the quality of training and test data sets. In this study, our training and test dataset consist of $\sim$ 95,000 and $\sim$70,000 clusters configurations and their energies for 54 different elements across the Periodic table, respectively. The sampled configurations contain (a) the ground state atomic structures (b) atomic structures near equilibrium and (c) structures far from equilibrium. A total of $\sim$ 19,000 ground state cluster configurations were evenly included amongst the training and test dataset. As a result, the DFT computed energies of sampled configuration generates a broad spectrum of energy window (ranging from $\sim$ 1 eV/atom, for alkali and alkali earth metals to $\sim$ 14 eV/atom, for non-metals) in the training and test data set. A continuous energy window from low to high for the sampled configurations ensures that the energetics and dynamics of clusters configurations starting from equilibrium to far-from-equilibrium are adequately represented. Ground state clusters configurations are mined from different literature [30] as well as from our own calculations using standard atomic structure prediction method (such as genetic algorithm [31, 32]). We used Boltzmann-based Metropolis sampling and a nested ensemble-based [33, 34, 35] approach to generate the cluster configurations that have energies near equilibrium and far from equilibrium. The combination of these two techniques generates cluster configurations of continuous range of energies from high to low. From the size perspective, the cluster configurations sampled consist of dimers to bulk-like configurations i.e., clusters containing atoms more than 50 atoms. Details on the various sampling approaches to generate cluster configurations are provided in Section 5 of Supplementary Information.

Reference Energy and Force Computations for Cluster Configurations

The energies of all the cluster configurations were computed using density functional theory (DFT) as implemented in the *Vienna Ab initio Simulation Package* (VASP) [36]. The low energy cluster configurations are further relaxed using conjugate gradient approach [37] whereas in the case of non-equilibrium cluster we perform static DFT calculation to compute their energies and forces. To avoid interactions between two periodic images we assign the box length such that the distance between two periodic images is at least 15 Å or larger. The DFT calculations were performed using the generalized gradient approximation (GGA) with the Perdew-Burke-Ernzerhof (PBE) exchange correlation functional, and the projected-augmented wave (PAW) pseudo-potentials [38]. The details of pseudo-potentials used in our calculations are provided in the Table 2 in Supplementary Information Section 4. Spin polarized calculations with the Brillioun zone sampled only at the Γ-point were performed. To handle errors that may arise during the structural relaxation or static DFT calculations, our high throughput workflow used an in-house python wrapper [39] around VASP along with a robust set of error handling tools.

Learning of Trial Functions

We performed a rigorous test using a series of trial functions to demonstrate the suitability of our c-MCTS approach. We use several popular test functions [40] which are designed to represent a wide variety of different continuous action surfaces. These surfaces include many local minima (Ackley, Buckley, Ragstrigin, etc.), misleading or non-existant gradients (Hyper Plane, Dejong Step Function), or other functions that are designed to mimic common optimization traps that one may encounter. An advantage of these functions is that they are computationally quick to evaluate and have known solutions. In addition, several of them can be scaled up to an arbitrary number of dimensions. As such, these trial functions provide a series of comprehensive first order tests to evaluate a search algorithm. These functions have implementations in a wide variety of programming languages such as Matlab, Python, R to name a few. We compare the performance of c-MCTS with several other global/local optimizers including evolutionary algorithms such as particle swarm, bayesian optimization and random sampling. For the particle swarm the PySwarm optimization package [41] was used with 50 particles per trial and the hyper parameters (c1, c2, w) were adjusted on a per trial basis starting from a default of (0.5, 0.3, 0.9). For the Bayesian based optimization the HyperOpt Python package [42] with the 'TPE. Suggest' option was used as the trial selection method.

The performance of the various optimizers on several different trial functions is listed in Extended Table 1 and the convergence to solution for representative cases is shown in Extended Figure 1.

Model Selection - Hybrid Bond Order Potential

We navigate a 18-dimensional potential energy surface represented by a hybrid bond order potential (HyBOP) expressed as

$$V = V_{SR} + V_{LR} \tag{2}$$

which utilizes a Tersoff formalism [43] for describing short range directional interaction (V_{SR}) and a scaled Lennard-Jones (LJ) function for long range interaction (V_{LR}). The short range pair potential function V_{pair} is described by

$$V_{SR} = \frac{1}{2}\sum_{i}\sum_{i\neq j} f_C(r_{ij})[f_R(r_{ij}) + b_{ij} f_A(r_{ij})] \tag{3}$$

where $f_C(r_{ij})$, $f_R(r_{ij})$, and $f_A(r_{ij})$ are the cutoff, repulsive, and attractive pair interactions, respectively, between bead i and j separated by a distance r_{ij}, and b_{ij} is a bond-order parameter which modifies the pair interaction strength between bead i and j depending on their local chemical environment. The long-range interactions V_{LR} uses a scaled Lennard-Jones (LJ) function which is given by,

$$V_{LR} = \sum_{i}\sum_{j>i} 4\epsilon_{ij} f_s(M_i)\Big[\Big(\frac{\sigma_{ij}}{r_{ij}}\Big)^{12} - \Big(\frac{\sigma_{ij}}{r_{ij}}\Big)^{6}\Big] \tag{4}$$

where, ϵ_{ij} and σ_{ij} are LJ parameters for a pair of atoms i and j that are a distance r_{ij} apart. $f_s(M_i)$ is a scaling function that describes the dependence of LR contribution from a given atomic pair $i-j$ on the number of atoms within a prescribed radial distance R_c^{LR} from the atom i. Details of the potential model are provided in the Supplementary Information Section 6. Owing to its flexibility in describing various bonding characteristics as well as to facilitate comparisons, we retain the HyBOP formalism across all the elements in the Periodic Table.

Learning of High-dimensional Potential Energy Surface

To navigate the high-dimensional continuous parameter space, we developed a workflow that interfaces the MCTS algorithm with a molecular simulator, large-scale atomic/molecular massively parallel simulator (LAMMPS) [44]. While MCTS is used to navigate the high-dimensional HyBOP parameters space, LAMMPS is used to evaluate the performance of a given input set of HyBOP parameters by computing the mean absolute error (MAE) of energies for the clusters in the training data set. Each node of the MCTS search represents a particular set of HyBOP parameters, with the reward r in Eq. 1 evaluated as the weighted sum of MAE error in the cluster energies as discussed in Supporting Information Section 7.1. MCTS is a decision tree-based approach (comprising of selection, expansion, simulation and back-propagation) that builds a shallow tree of nodes where each node represents a point in the search space and downstream pathways are generated by a playout procedure. The algorithm simultaneously explores potentially better pathways to reach the optimal point in a search space and exploits a subset of pathways that have the greatest estimate values of the search function. This combination of exploration vs exploitation and an appropriate trade-off mechanism between them are found to be the most efficient strategy of identifying optimal point for a given function. The details of the c-MCTS approach are provided in the Supporting Information.

Fingerprinting and Principal Component Analysis

To analyze the structural diversity of the cluster dataset across the different elements, we utilized the smooth overlap of atomic positions (SOAP) fingerprinting method [26] as implemented in the DScribe python library [45]. SOAP encodes the atomic neighbourhood around a spatial point (or an atom) using the local expansion of a Gaussian smeared atomic density with orthonormal basis functions composed of spherical harmonics and radial basis functions. The advantage of using the SOAP fingerprint is that it is invariant to translation, rotation and permutations of alike atoms of a configuration, and forms the basis for development

of several successful ML-based inter-atomic potentials. The following parameter settings were used for the SOAP fingerprinting: rcut= 6Å, nmax= 6 and lmax= 4, where rcut is the cut-off radius for the atomic neighborhood around the concerned atom, namx is the number of radial basis functions (spherical Gaussian type orbitals) and lmax is the maximum degree of spherical harmonics. This resulted in a SOAP fingerprint vector for each atom, which was averaged using the "inner" averaging scheme (average over atomic sites before summing up the magnetic quantum numbers) to obtain a 105-dimensional configuration fingerprint for each cluster. Principal component analysis (PCA) was performed using the (standard) normalized SOAP fingerprint representation of the entire cluster dataset. The variance in energy changes as a function of SOAP fingerprint distances (cosine) was computed using the open-source Scikit-GStat Python library [27].

Extended Data

Extended Table 1: Performance comparison among c-MCTS, Bayesian, particle swarm, and random sampling methods to find optimal solutions in 25 different trial functions. Two performance metrics were chosen: the number of iterations to reach the target solution and the quality of the best solution obtained from the optimizer. Results up to a maximum of 30000 iterations are provided. D denotes the dimension of the trial function, while the tolerance indicates the accepted difference from the exact optimal solution of the trial function. Bold font highlight the winning solution in each row.

				c-MCTS		Bayesian		Particle Swarm		Random	
Trial Function	D	Exact Solution	Tolerance	# of Iterations	Best Solution	# of Iterations	Best Solution	# of Iterations	Best Solution	# of Iterations	Best Solution
Ackley	2	0.000	1.000	269	0 ± 0.0	**146**	**0.6±0.125**	167	0±0	687	1.198 ±0.515
Ackley	4	0.000	1.000	601	0 ± 0.0	803	2.743 ± 0.342	**507**	**0±0**	>30000	6.854 ± 3.071
Ackley	10	0.000	1.000	**601**	**0.001 ± 0.0**	>30000	6.408 ± 0.573	1372	0.0 ± 0.0	>30000	15.802 ± 1.205
Ackley	15	0.000	1.000	**601**	**0.002 ± 0.0**	>30000	10.604 ± 1.435	1814	0.635 ± 0.426	>30000	17.869 ± 0.471
Ackley	30	0.000	1.000	**601**	**0.005 ± 0.0**	>30000	16.466 ± 0.0	>30000	4.2 ± 0.847	>30000	19.777 ± 0.036
Ackley	50	0.000	1.000	**601**	**0.002 ± 0.0**	>30000	18.354 ± 0.052	15072	4.287 ± 0.625	>30000	20.304 ± 0.014
Damavandi	2	0.000	1.000	**2821**	**0.0207 ± 0.001**	>30000	2.0 ± 0.0	>30000	2.0 ± 0.0	29761	0.437 ± 0.156
Dixon Price	13	0.000	1.000	**9482**	**0.605 ± 0.043**	>30000	1.542 ± 0.0	5758	0.705 ± 0.01	>30000	20680.725 ± 64499917.399
EggHolder	2	-959.000	1.000	**13025**	**-959.364 ± 0.665**	>30000	-937.074 ± 930.271	>30000	-950.075 ± 89.247	>30000	-948.275 ± 50.051
Levy	2	0.000	1.000	7217	0.626 ± 0.068	**21**	**0.0 ± 0.0**	>30000	90.994 ± 768.539	>30000	2748.049 ± 30219.815
Schwefel	3	0.000	0.100	13277	0.029 ± 0.001	>30000	4.196 ± 451.225	**4964**	**0.0 ± 0.0**	>30000	0.124 ± 0.009
HyperRastrigin	2	0.000	5.000	115	0.013 ± 0.001	**74**	**0.41 ± 0.251**	133	0.0 ± 0.0	139	0.246 ± 0.044
HyperRastrigin	9	0.000	5.000	**5215**	**0.997 ± 0.0**	>30000	431.285 ± 338.013	>30000	116.225 ± 577.774	>30000	637.065 ± 347.21
HyperRastrigin	50	0.000	5.000	**5307**	**1.0 ± 0.0**	>30000	436.267 ± 129.964	>30000	11.356 ± 11.788	>30000	97.939 ± 62.296
Dejong	2	0.000	0.001	**821**	**0.0 ± 0.0**	>30000	1.1 ± 0.09	>30000	0.033 ± 0.032	171162	0.0 ± 0.0
Dejong	9	0.000	0.001	**1985**	**0.0 ± 0.0**	>30000	3.467 ± 0.249	>30000	12.4 ± 4.507	>30000	15.333 ± 8.089
Dejong	15	0.000	0.001	**2386**	**0.0 ± 0.0**	>30000	11.2 ± 1.56	>30000	31.733 ± 17.929	>30000	37.033 ± 25.499
Dejong	50	0.000	0.001	**4968**	**0.0 ± 0.0**	>30000	103.333 ± 66.889	>30000	158.167 ± 142.339	>30000	189.933 ± 33.796
Dropwave	2	-1.000	0.010	**2369**	**-0.998 ± 0.0**	>30000	-0.976 ± 0	2979	-1.0 ± -0.0	>30000	-0.972 ± 0.001
Nestorov	13	0.000	1.00E-07	>30000	0.21 ± 0.017	>30000	2.198 ± 0.1	>30000	0.318 ± 0.039	>30000	5.513 ± 0.353
Grammacy & Lee	1	-0.869	1.00E-07	**235**	**-0.869 ± 0**	2105	-0.869 ± 0.0	>30000	-0.869 ± 0.0	10964	-0.869 ± 0.0
HyperPlane	2	-5.120	1.000	**14**	**-5.12 ± 0.0**	23	-4.718 ± 0.113	98	-5.078 ± 0.001	60	-5.05 ± 0.001
HyperPlane	9	-5.120	1.000	1050	-5.12 ± -0.0	**404**	**-5.01 ± 0.0**	>30000	-3.629 ± 0.056	>30000	-3.701 ± 0.054
HyperPlane	15	-5.120	1.000	**1246**	**-5.114 ± 0.001**	3578	-4.682 ± 0.002	>30000	-2.909 ± 0.171	>30000	-2.925 ± 0.017
HyperPlane	50	-5.120	1.000	**2360**	**-5.102 ± 0.001**	>30000	-3.413 ± 0.0	>30000	-2.357 ± 0.043	>30000	-1.687 ± 0.006

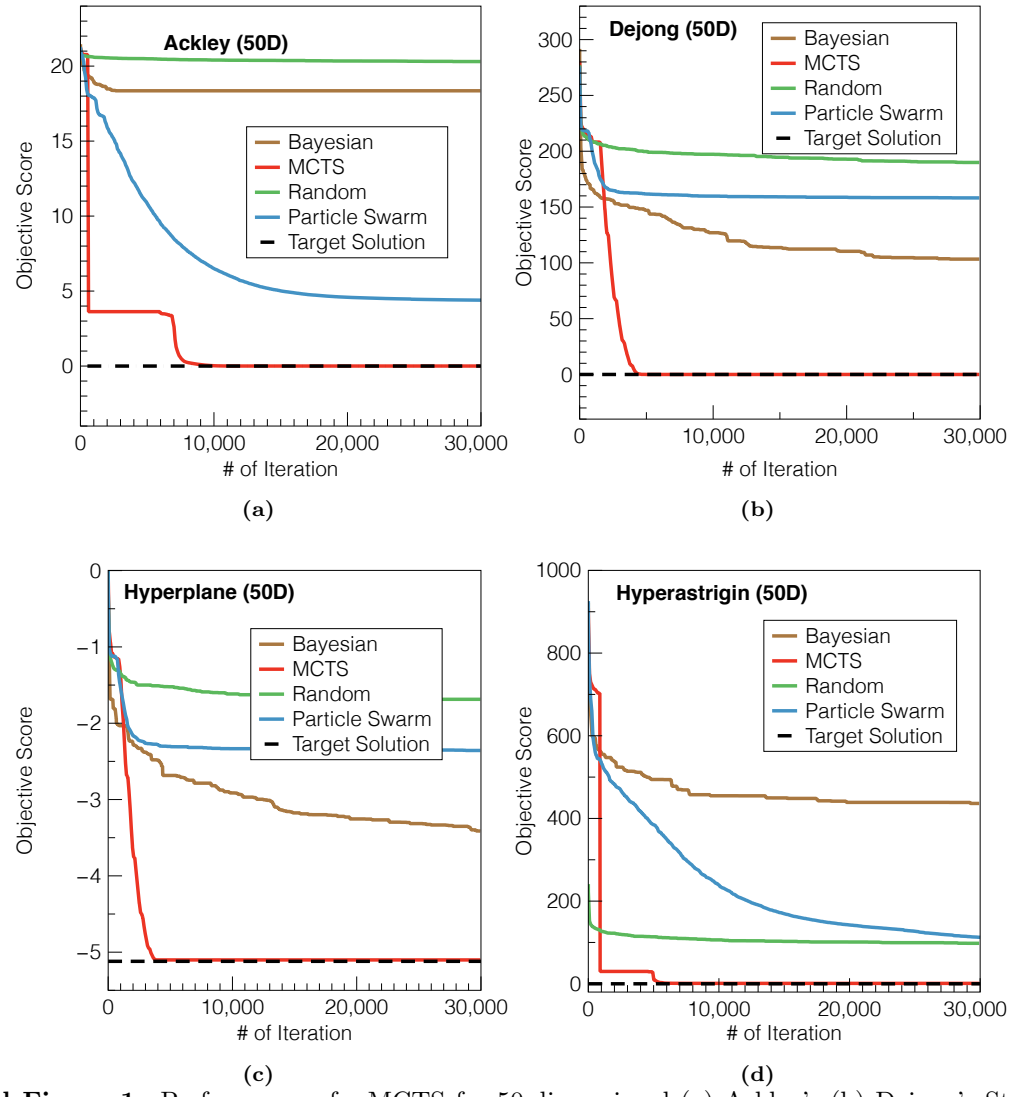

Extended Figure 1: Performance of c-MCTS for 50-dimensional (a) Ackley's (b) Dejong's Step (c) Hyperplane and (d) Hyperrastrigin functions. In all cases, c-MCTS outperforms other optimizers both in terms of the number of iterations to reach the solution and the quality of the best solution.

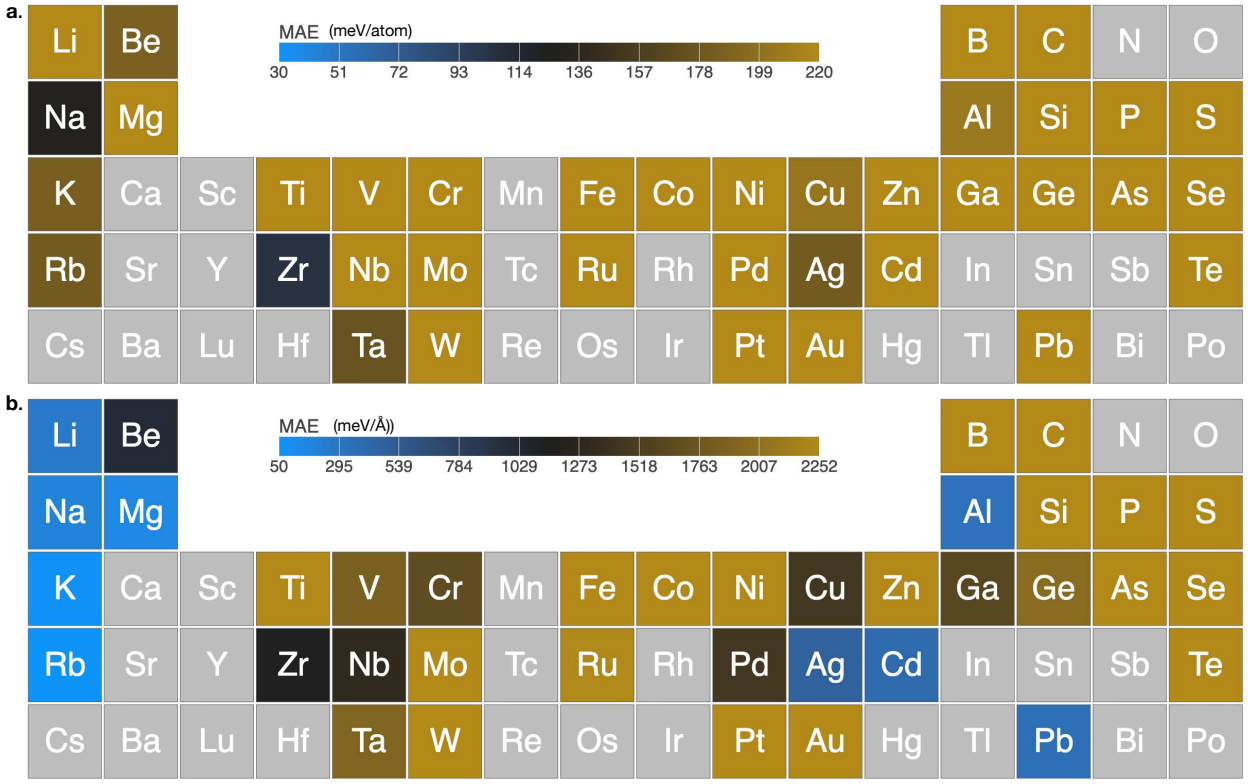

Extended Figure 2: Performance of the best available force fields collected from literature on predicting energies and forces of different elemental cluster configurations. For better error comparison with Figure 2, consistent error range and color scheme are used. Elements for which comparison studies were omitted are colored grey. More rigorous performance evaluations (for both energies and forces) covering a wider range of popular force fields can be found in Section 5 in the Supplemental Information.

Extended Table 2: c-MCTS optimized parameters for all 54 elements based on the Hybrid Bond-Order Potential formalism. While all 19 parameters are included here, we note that the parameter m was kept constant during the c-MCTS.

Element	m	γ	λ_3 (Å^{-1})	c	d	h	n	β (eV)	λ_2 (Å^{-1})	B (eV)
	R (Å)	D (Å)	λ_1 (Å^{-1})	A (eV)	ϵ (eV)	σ (Å)	κ_1	κ_2	R_c^{LR}	
Ag	1.0	0.439004132	2.081215	299830.887	496.9692108	-0.283814359	1.254540539	0.577719735	1.301999873	67.91828712
	4.527969417	0.776211611	3.146003288	3347.691344	0.480327194	1.8998194	87.37014716	2.264557099	9.649360956	
Al	1.0	0.61326995	1.390807006	206728.4214	547.6951546	-0.409328744	0.586298228	0.547650551	1.095687614	67.74558273
	4.904788169	0.966678745	2.766703214	1272.396803	0.315475527	2.750566828	98.3112166	3.614864665	8.56676085	
As	1.0	1.106244146	2.884304258	65223.88438	308.1048407	-0.563380956	1.342579919	0.559130447	1.227024981	100.6111088
	3.401637287	0.58323519	2.917644724	2179.071075	0.265131013	3.28758861	55.0250877	9.045779104	13.4060757	
Au	1.0	0.540184679	1.55210473	32709.11482	317.1653606	0.297478562	0.804091077	0.65383625	1.268620424	83.30626228
	4.456082718	0.613184263	3.30339905	5668.65435	1.291224079	2.484037292	86.51252656	5.334187157	11.80323209	
B	1.0	0.471737346	1.958698013	17303.90172	98.49490145	-1.601276844	2.588982161	0.120603008	1.21032307	42.68956511
	2.689202772	1.075218182	3.761527212	844.2957697	0.093267	1.583298	78.2364	2.7259	9.036302	
Ba	1.0	1.080429781	2.197	54053.44342	757.9563559	0.091677874	1.325812836	0.569926462	0.01238515	0.885917927
	5.613391625	1.103671746	2.386872518	1378.553718	0.965764	2.497763	72.6924	1.4554	11.037448	
Be	1.0	0.389322938	0.554376294	144255.5747	686.139186	0.02274642	1.182029373	0.122285965	1.757902066	48.50631693
	3.513963888	0.578399955	3.600194036	798.7204114	0.037022	2.2832	58.7876	0.6999	11.11013	
Bi	1.0	0.428842935	1.762335078	136185.8192	282.8821816	-0.154665	1.486131241	1.096823628	0.927192609	52.61997211
	3.819974038	1.341637421	2.814392264	4213.936014	0.523803	2.226705	46.1600	6.6549	9.782088	
C	1.0	1.356341544	1.325014828	172558.8946	259.030336	-1.024062133	1.274996013	0.073875782	1.237579216	72.069305
	1.914491402	1.173101798	3.553365135	645.54068	0.198195271	2.530738424	94.0835042	9.108572273	8.797646976	
Ca	1.0	0.601021859	1.68855454	84072.63094	541.0676661	0.0250954	1.341695877	0.204708236	0.679774753	7.305849158
	5.497807288	1.253721854	2.830294691	4659.512322	0.104062639	2.422769663	53.89038493	5.165081808	10.2350796	
Cd	1.0	1.373903135	3.171310137	149186.9592	813.7241335	-0.935908093	0.763500877	0.007712742	1.719081756	48.60324077
	3.341765009	0.735708505	3.645203574	8668.575744	0.224392209	3.084920374	35.86897909	6.212665025	8.891974	
Co	1.0	2.018582792	0.493139267	80694.34818	426.3412213	-0.384391039	0.769860607	0.68803926	0.426205112	13.59954812
	3.200504248	1.139856984	3.569969101	1223.654439	0.712191921	2.546677283	90.27443323	5.989507871	9.604259394	
Cr	1.0	1.92795542	1.7671341	1119883.517	5221.57347	-0.399398021	1.165667229	0.535819241	1.112386068	76.8392884
	4.504818329	0.298300173	3.102805518	932.6629025	0.486637	2.361382	92.3655	7.3694	11.923865	
Cs	1.0	1.41192758	-0.594485472	78880.54739	587.9518475	0.342520639	1.611704147	2.82E-07	0.291398126	0.748992305
	6.205049779	0.864691614	2.408972612	5179.457988	0.072900881	3.132467505	26.70759923	0.997328444	12.64727929	
Cu	1.0	1.980852481	-0.018161201	198952.0274	392.3384758	-0.473107091	0.456987926	0.268096204	1.069379843	56.92693813
	3.935778112	0.866449238	3.696412894	2495.524952	0.281895956	2.70053134	91.1371509	8.64756679	13.49371528	
Fe	1.0	1.348803356	1.131690664	125033.9361	984.4901492	-0.259638411	1.281306674	1.362859335	0.65108477	36.53924165
	3.85107905	0.937046269	3.048350721	798.8657954	0.199181714	2.960363905	66.37455175	9.730524066	10.96653145	
Ga	1.0	0.335734826	3.471330188	272466.9786	460.9757712	-0.616594581	0.865522121	0.682852796	1.162583267	56.15376023
	4.192036967	0.94667352	2.929695689	1363.339421	0.870039287	2.880120134	55.68070898	7.537198109	9.821670567	
Ge	1.0	1.592848631	0.55062431	127524.3878	424.2159922	-0.401269633	1.435117334	0.469540896	1.061831856	54.30648823
	3.420435009	0.398005685	3.695443654	6282.806413	0.489924233	3.497502639	80.30992939	6.755374181	13.57379685	
Hf	1.0	0.537087031	-0.645372326	282074.3915	625.5649075	-0.525559262	1.293372245	0.529141922	0.635009172	17.86215975
	4.193246955	1.162261159	3.433042224	2207.798866	0.064317644	2.757840692	47.72151412	4.202250839	11.562887	
In	1.0	1.18003807	1.971969108	104714.9588	541.0974275	-0.017707181	0.715906464	0.711710569	0.907676898	44.78258893
	4.16275743	0.248455146	2.708250568	1779.665973	0.019035	3.125197	62.9797	2.2415	8.165851	
Ir	1.0	1.515170714	2.501558073	249903.8071	441.9181724	-0.380968138	0.891345414	0.373009713	0.677890537	32.87769716
	3.786398208	0.521033474	3.383311321	3435.277077	0.09592166	2.53532036	27.4032917	9.986981587	10.58588337	
K	1.0	0.190890139	1.422255329	93845.15611	520.0165729	0.021264581	1.576238686	0.089956024	0.152328952	0.330090427
	5.885945343	0.307614421	3.145111298	836.3684338	0.37815361	3.018136796	33.88116219	7.943089064	11.95182157	
Li	1.0	0.403658365	1.574524438	153077.961	835.8136338	0.21833845	0.696339874	0.176248356	1.31019501	39.66576204
	4.282364887	0.539653843	2.763332616	948.2953131	0.278142038	3.280998076	61.50569789	8.782786468	14.34966638	
Mg	1.0	1.480006192	2.571519383	1.0	718.7902675	-0.292064506	0.904666562	1.00E-12	0.830252339	3.697426365
	4.332071305	0.923157887	3.590121995	4820.643508	0.539040509	3.227777521	81.07550467	4.32014228	12.01785776	
Mn	1.0	0.691663261	2.77539634	235036.1528	539.3090631	-0.858423468	0.780540164	0.36574435	0.158299208	2.153754752
	4.655357915	0.217	3.638516335	751.8356469	0.234414532	2.620170677	76.42004885	8.089526669	13.35110289	

Element	m	γ	λ_3 (Å^{-1})	c	d	h	n	β	λ_2 (Å^{-1})	B (eV)
	R (Å)	D (Å)	λ_1 (Å^{-1})	A (eV)	ϵ (eV)	σ (Å)	κ_1	κ_2	R_c^{LR}	
Mo	1.0	1.064431285	3.224568877	45525.3245	548.8403	-0.828290799	1.001685715	0.689636271	1.089461796	100.0
	3.871329492	0.827104827	2.837306147	1234.479192	0.328548	1.48957	37.6889	5.2976	12.55871	
Na	1.0	0.286672007	1.496885877	6051.492309	536.5634878	-0.394761259	0.379586185	0.345311286	0.758507628	7.057994713
	4.39268266	0.883447271	3.385067448	2977.082688	0.781829997	2.999467142	35.7584234	8.333700039	10.95074377	
Nb	1.0	1.605692851	1.045170744	20586.31782	596.7623982	1.078795456	0.588359781	0.638479854	0.984270828	93.42058233
	3.614261629	0.45916404	3.603718521	8192.397635	0.131135143	3.473509559	100.0	7.267820478	11.96203672	
Ni	1.0	1.633132766	2.550007224	269763.271	812.5835119	-0.265790302	0.770166985	0.662147668	0.981654449	50.68472708
	3.782335152	1.173649804	3.657281569	2563.146872	0.471802281	3.303197639	44.89532908	7.57728473	8.09611573	
Os	1.0	0.201012041	1.60889609	57499.75116	219.998652	-1.755431765	1.396875848	0.63920147	0.78686991	41.08896918
	5.616030793	0.406133817	3.289373554	3790.748951	0.147402685	2.421082681	42.6219374	8.819753789	12.61122667	
P	1.0	0.817636314	0.990814767	88656.223	234.5704413	-0.069401968	1.21831237	1.024415214	1.074725703	60.44157271
	2.648240705	0.907473275	3.65221791	3268.035577	0.1	4.172088	104.3823	4.3652	8.079076	
Pb	1.0	1.145021612	0.691696985	299791.85	534.7073248	0.266861213	1.113867118	0.740240453	0.524214715	13.53564362
	4.517005421	0.338926208	3.204191428	4919.256364	0.983028724	2.516372875	85.97972499	4.63503069	12.13131791	
Pd	1.0	0.9921444	0.59359854	214931.6366	738.3965827	0.617858241	0.289801643	0.648150217	0.754711276	37.53770302
	4.886222734	0.897676349	3.324006014	2436.347635	0.570708655	2.679900418	68.51300145	5.975332666	10.91632761	
Pt	1.0	2.285489564	1.290577486	199007.334	445.1252682	-0.217482552	0.700743835	0.763369527	0.64281201	38.48646614
	5.57149324	0.407983178	3.400939359	4571.376172	0.438212734	2.525224881	98.93969405	2.958248513	10.29412317	
Rb	1.0	0.813939364	-0.145613799	138756.0431	565.6565871	0.536127522	0.249781792	0.112708772	0.286361733	2.234995775
	6.227770735	0.761403772	2.844380268	5534.773143	1.0	2.016776668	21.73110002	9.674104476	13.69306627	
Re	1.0	0.867220063	1.649489919	276148.7476	561.7919931	-0.875774608	0.92615311	0.239554639	1.032695972	67.6703742
	3.454534619	0.672961801	2.940389386	1901.018145	0.213364379	2.554547196	44.11165545	4.501812369	12.98535097	
Rh	1.0	1.420419655	2.562464109	99907.15431	647.1237206	-0.140395259	0.487526958	0.744704577	0.891796417	71.22389368
	4.549726836	0.178738264	3.044738951	1763.860904	0.059255986	2.321283774	96.04428903	3.16118168	10.41516111	
Ru	1.0	1.13885549	2.530803076	79980.38686	325.1522123	-0.554512049	1.022441078	1.097620425	0.620331197	28.69858397
	4.101837952	0.501123867	3.802725511	3140.19991	0.265456711	2.432516346	41.10622697	5.893489595	12.95931994	
S	1.0	2.80695877	3.303382406	2482005.407	6442.218436	-0.671107922	2.366321206	0.672278112	1.57753987	210.6857932
	3.426755389	0.558784629	3.621667726	4722.126813	0.004606265457953138	2.6202183740992497	49.762933451668495	3.132576961132626	8.376319319339993	
Sb	1	1.205796288	3.428212262	164753.5862	286.9578608	-0.144	1.675228883	0.699835507	0.905019663	42.01677545
	4.028566448	1.228351588	3.586686372	12524.14456	0.136717859	3.029951717	97.37818014	1.116639675	9.969802129	
Sc	1.0	1.856944766	2.816624988	42210.63695	599.889996	-0.014750005	0.860684276	0.483840607	0.000377392	2.307771854
	3.944024934	0.482030036	3.989837195	1102.806886	0.392490906	3.261366341	28.00422914	6.566777067	8.758442475	
Se	1	1.866945434	5.284134295	379460.4323	516.990327	-0.268654474	1.477779591	1.078911787	0.906930171	51.88255152
	4.397167131	0.284496726	3.470374266	4635.370239	0.475441	2.914816	71.4525	5.5353	10.814723	
Si	1.0	1.161046328	1.430520338	84700.08413	287.7858849	-0.2142454	1.188595521	0.606216451	0.876818864	41.7700433
	2.975881529	0.596704237	3.113372791	1638.992828	1.0	3.338374359	100.0	7.970283456	13.67484445	
Sn	1.0	1.075789457	2.472553968	234035.3107	998.579802	0.219905615	0.865481782	0.695145199	0.983205941	86.77134569
	3.984126032	1.190260828	2.43387035	1602.516257	0.034352	3.789084	65.4019	3.5848	12.148124	
Sr	1.0	0.002874677	-0.279905101	229975.946	196.9516313	0.739609926	1.846769386	0.350110848	1.080722827	41.1383277
	6.054550855	0.730957664	2.533302713	6198.226751	0.540459827	2.383357541	59.60493972	3.939678539	11.40402495	
Ta	1.0	1.994875649	0.356071016	37960.9261	270.3334767	-0.200500861	0.48434717	0.396769923	0.740661737	77.77514435
	3.549672448	1.087491645	2.174766918	472.6500557	0.894446254	3.5	56.46748141	9.010987909	12.95070214	
Te	1.0	1.187106601	2.058430258	42194.36619	166.4670169	-0.282285175	1.64557754	1.049863864	0.816193966	42.73690089
	3.337707472	0.695473313	3.074997403	4914.854691	0.036836939	3.115980692	21.87488961	2.23394627	9.34551566	
Ti	1.0	2.041642677	0.76985604	31609.18119	459.6970893	1.000031178	0.49527892	0.730661855	0.609286739	25.87802924
	3.752769081	0.756737846	3.744686874	2697.709163	0.117965854	2.833069485	36.10915399	0.964111804	8.434791183	
Tl	1.0	1.861481018	1.024619449	177004.4707	562.837062	-0.838850776	0.87049895	0.527144758	0.491724128	9.876005883
	4.518570476	0.517724204	2.926894875	1981.856132	0.620039064	1.829123761	33.30019543	3.918525243	11.74147777	
V	1.0	0.828248904	1.868252124	105338.7485	336.7584392	-0.555850048	0.767880226	0.448133891	0.889855294	55.06877235
	3.945888512	0.534293061	2.206520942	297.8565742	0.653741435	1.653056402	25.19483873	8.871708141	9.147797078	
W	1.0	1.733281453	0.889495756	38400.6511	672.1917599	0.175986316	0.931894395	0.327854969	0.981151321	70.97303351
	4.696003567	0.711584029	3.027666244	1889.790063	0.871266328	3.5	63.22564091	4.352595505	8.188309126	
Y	1.0	1.722353735	-0.762827663	56836.22713	340.5570259	0.298384897	0.7271999	0.361694379	1.00E-12	2.147458895
	4.380369471	1.07179749	3.617481558	7085.718235	0.320196693	1.358081976	24.83542283	2.205687823	9.990132728	
Zn	1.0	0.083237527	0.820750759	78930.88677	936.397098	0.640748578	1.513753004	0.305554579	1.969551617	67.47220176
	3.814394367	0.85887803	3.811646873	4806.582051	1.326085473	3.643981213	66.96283645	5.304692743	7.340658374	
Zr	1.0	0.902476081	0.336486599	100111.1357	798.3309379	-0.333348522	1.386597527	1.100484953	0.381386763	11.32613901
	3.70592479	0.323222298	4.037608214	11461.40433	0.037644637	3.256534514	20.67028522	2.596271152	8.925563713	

Extended Table 3: Predicted cohesive energies of $\sim$ 200 different polymorphs of 54 different elements from c-MCTS optimized hybrid bond order potential parameters. The bulk structures have been collected from materials project database [46]. The calculated DFT predicted properties have been evaluated using same VASP settings as for evaluating energies for nanoclusters. Details are provided in the Supplementary Information section 4.

Element	Crystal Structure or Space Group	Cohesive Energy [DFT] (eV/atom)	Cohesive Energy [HyBOP] (eV/atom)	Element	Crystal Structure or Space Group	Cohesive Energy [DFT] (eV/atom)	Cohesive Energy [HyBOP] (eV/atom)
Ag	fcc	-2.511725	-2.678527	Ga	64	-2.709715	-2.77013
Ag	bcc	-2.486285	-2.662565	Ga	63	-2.70549	-2.737447
Ag	hcp	-2.466516	-2.641534	Ga	166	-2.700409	-0.923209
Ag	dc	-1.740683	-1.968567	Ge	dc	-3.727929	-3.161135
Al	fcc	-3.550967	-3.678654	Ge	hcp	-3.437855	-3.044477
Al	hcp	-3.482888	-3.665045	Ge	fcc	-3.408915	-2.949522
Al	bcc	-3.418648	-3.649364	Ge	bcc	-3.396594	-2.510756
Al	dc	-2.787166	-2.666609	Hf	hcp	-6.424324	-6.923274
As	166	-2.976068	-2.905794	Hf	fcc	-6.412572	-6.920017
As	64	-2.956048	-2.755563	Hf	bcc	-6.30179	-6.786385
Au	fcc	-3.039523	-3.110927	Hf	dc	-3.797874	-4.723101
Au	bcc	-3.016642	-3.077583	In	225	-2.398108	-2.451924
Au	hcp	-2.968084	-3.021436	In	139	-2.390626	-2.444852
Au	dc	-2.334834	-1.97954	In	194	-2.375204	-2.446356
B	166	-6.411857	-6.777673	Ir	fcc	-7.438913	-8.100696
B	58	-6.374528	-6.829759	Ir	hcp	-7.406411	-8.010652
Ba	bcc	-1.898709	-1.950853	Ir	bcc	-6.801922	-7.766919
Ba	fcc	-1.878124	-1.891708	Ir	dc	-6.403451	-5.695726
Ba	hcp	-1.835984	-1.889814	K	bcc	-0.815316	-1.448568
Ba	dc	-0.931932	-0.852879	K	hcp	-0.811026	-1.391862
Be	hcp	-3.678366	-3.457156	K	fcc	-0.808695	-1.333891
Be	fcc	-3.648624	-3.45592	K	dc	-0.568378	-1.108746
Be	bcc	-3.643434	-3.383279	Li	bcc	-1.602626	-1.460418
Be	dc	-2.0921	-1.508473	Li	hcp	-1.599063	-1.441768
Bi	166	-2.545872	-2.466887	Li	fcc	-1.594919	-1.342393
Bi	221	-2.501312	-2.443583	Li	dc	-1.087183	-1.005804
Bi	11	-2.499945	-2.440143	Mg	hcp	-1.508292	-1.431628
C	194	-8.085643	-7.691359	Mg	fcc	-1.488512	-1.422104
C	dc	-8.04232	-7.648072	Mg	bcc	-1.473176	-1.418283
Ca	fcc	-1.904007	-1.791543	Mg	dc	-0.742313	-0.717385
Ca	bcc	-1.865393	-1.77714	Mo	bcc	-7.868566	-7.299034
Ca	dc	-0.870288	-0.848194	Mo	fcc	-7.437533	-7.236264
Cd	hcp	-0.805063	-0.501228	Mo	hcp	-7.305558	-7.203089
Cd	fcc	-0.719304	-0.491894	Mo	dc	-5.690853	-5.601266
Cd	bcc	-0.660937	-0.454511	Mn	213	-3.825298	-4.13521
Cd	dc	-0.419069	-0.182275	Mn	dc	-2.509528	-2.802293
Co	hcp	-5.495889	-5.48542	Na	bcc	-1.081903	-1.087598
Co	bcc	-5.4624	-5.482344	Na	fcc	-1.065422	-1.043722
Co	fcc	-5.383827	-5.480283	Na	hcp	-0.943856	-0.900545
Co	dc	-4.289325	-4.286697	Na	dc	-0.743367	-0.547226
Cr	bcc	-7.146919	-6.451581	Nb	bcc	-7.117227	-6.800298
Cr	fcc	-6.736178	-6.387226	Nb	fcc	-6.780568	-6.667064
Cr	hcp	-6.646299	-6.340389	Nb	hcp	-6.7343	-6.503295
Cr	dc	-5.068723	-5.587453	Nb	dc	-4.566032	-4.392304
Cu	fcc	-3.484558	-3.51709	Ni	fcc	-5.561355	-5.191993
Cu	hcp	-3.481414	-3.514532	Ni	hcp	-5.540381	-5.113854
Cu	bcc	-3.455087	-3.492064	Ni	bcc	-5.481357	-5.074967
Cu	dc	-2.48237	-2.034938	Ni	dc	-4.3766	-4.104433
Fe	bcc	-7.635909	-7.555372	Os	hcp	-8.222873	-9.319432
Fe	hcp	-7.539061	-7.555037	Os	fcc	-8.178825	-9.319391
Fe	fcc	-7.504575	-7.543839	Os	bcc	-7.407289	-9.258629
Fe	dc	-6.432157	-6.05063	Os	dc	-7.084982	-6.590547

Element	Crystal Structure or Space Group	Cohesive Energy [DFT] (eV/atom)	Cohesive Energy [HyBOP] (eV/atom)	Element	Crystal Structure or Space Group	Cohesive Energy [DFT] (eV/atom)	Cohesive Energy [HyBOP] (eV/atom)
P	2	-3.523668	-3.175458	Sr	fcc	-1.614341	-1.693771
P	13	-3.518213	-3.141145	Sr	bcc	-1.613174	-1.68943
P	53	-2.603751	-3.064313	Sr	hcp	-1.604187	-1.688577
Pb	fcc	-3.002566	-3.258758	Sr	dc	-0.654009	-0.600016
Pb	hcp	-2.958443	-3.201885	Ta	bcc	-8.188406	-7.261214
Pb	bcc	-2.943543	-3.198847	Ta	fcc	-7.938669	-7.038726
Pb	dc	-2.709097	-2.087622	Ta	hcp	-7.721448	-6.802617
Pd	fcc	-3.756993	-3.851315	Ta	dc	-5.334876	-5.337801
Pd	bcc	-3.713697	-3.824644	Te	152	-2.487637	-2.323882
Pd	hcp	-3.708835	-3.817314	Te	51	-2.454671	-2.309573
Pd	dc	-2.637883	-2.446031	Te	26	-2.453546	-2.306971
Pt	fcc	-5.683154	-7.248088	Te	12	-2.450184	-2.303554
Pt	bcc	-5.557434	-7.213583	Te	221	-2.448225	-2.297885
Pt	hcp	-5.507283	-7.020244	Te	166	-2.44718	-2.289804
Pt	dc	-4.627776	-4.567044	Ti	hcp	-5.46973	-5.659291
Rb	hcp	-0.779024	-0.847858	Ti	fcc	-5.458149	-5.656921
Rb	fcc	-0.778202	-0.846446	Ti	bcc	-5.414838	-5.601304
Rb	bcc	-0.776903	-0.844636	Ti	dc	-3.405656	-2.8036
Rb	dc	-0.513786	-0.373211	Tl	hcp	-2.087312	-2.756243
Re	hcp	-7.773664	-8.893102	Tl	bcc	-2.085762	-2.674979
Re	fcc	-7.717929	-8.892743	Tl	fcc	-2.058703	-2.618666
Re	bcc	-7.471534	-8.766693	Tl	dc	-1.709524	-1.735913
Re	dc	-6.249314	-5.837517	V	bcc	-6.466928	-6.837281
Rh	fcc	-6.259331	-6.274332	V	fcc	-6.190417	-6.563272
Rh	hcp	-6.204678	-6.244817	V	hcp	-6.072358	-6.552652
Rh	bcc	-5.897166	-6.21429	V	dc	-4.220457	-5.587481
Rh	dc	-5.174197	-4.734084	W	bcc	-8.894151	-6.709545
Ru	hcp	-7.834005	-9.589588	W	fcc	-8.402234	-6.683261
Ru	fcc	-7.591943	-9.578795	W	hcp	-8.311161	-6.548693
Ru	bcc	-7.059656	-9.405646	W	dc	-6.279032	-5.344618
Ru	dc	-6.581176	-6.205775	Y	hcp	-4.168051	-4.00342
S	148	-3.179345	-3.034035	Y	fcc	-4.155554	-4.001346
Sb	166	-2.707282	-2.770084	Y	bcc	-4.049993	-4.075835
Sb	221	-2.673574	-2.734482	Y	dc	-2.227476	-2.628001
Sb	11	-2.658342	-2.721367	Zn	hcp	-1.101668	-0.800384
Sc	hcp	-4.194866	-4.080402	Zn	fcc	-1.062862	-0.760212
Sc	fcc	-4.176286	-4.079651	Zn	bcc	-1.025388	-0.587054
Sc	bcc	-4.12053	-4.077934	Zn	dc	-0.652028	-0.405924
Sc	dc	-2.277429	-2.273836	Zr	hcp	-6.289619	-5.861875
Se	152	-2.722448	-2.734832	Zr	fcc	-6.240104	-5.857419
Se	148	-2.702012	-2.362418	Zr	bcc	-6.180042	-5.823846
Si	dc	-4.592794	-4.1469	Zr	dc	-3.917309	-3.412517
Si	hcp	-4.088662	-3.97333				
Si	bcc	-4.072694	-3.744391				
Si	fcc	-4.061759	-3.430897				
Sn	139	-3.13455	-2.864157				

Extended Table 4: Predicted lattice parameters of $\sim$ 200 different polymorphs of 54 different elements from c-MCTS optimized hybrid bond order potential parameters.

Element	Crystal Structure or Space Group	a [DFT] (Å)	a [HyBOP] (Å)	b [DFT] (Å)	b [HyBOP] (Å)	c [DFT] (Å)	c[HyBOP] (Å)	α [DFT] (degree)	α [HyBOP] (degree)	β [DFT] (degree)	β[HyBOP] (degree)	γ [DFT] (degree)	γ [HyBOP] (degree)
Ag	fcc	4.106	4.109	4.106	4.11	4.106	4.109	90	90	90	90	90	90
Ag	bcc	3.262	3.262	3.262	3.262	3.262	3.262	90	90	90	90	90	90
Ag	hcp	2.941	2.935	2.941	2.933	9.313	9.434	90	90.2	90	89.8	120	120
Ag	dc	6.153	6.173	6.153	6.179	6.153	6.174	90	90	90	90	90	90
Al	fcc	4.049	4.077	4.049	4.077	4.049	4.077	90	90	90	90	90	90
Al	hcp	2.998	2.95	2.998	2.95	8.716	9.096	90	90	90	90	120	120
Al	bcc	3.241	3.251	3.241	3.251	3.241	3.251	90	90	90	90	90	90
Al	dc	6.048	6.002	6.048	6.002	6.048	6.002	90	90	90	90	90	90
As	166	3.803	3.836	3.803	3.828	10.781	10.522	90	90	90	90	120	119.8
As	64	5.966	6.671	5.966	5.636	4.464	4.341	90	77.7	90	93	143.191	130.3
Au	fcc	4.136	4.154	4.136	4.154	4.136	4.154	90	90	90	90	90	90
Au	bcc	3.279	3.302	3.279	3.302	3.279	3.302	90	90	90	90	90	90
Au	hcp	3.081	3.062	3.081	3.067	8.652	8.898	90	90	90	90	120	120.2
Au	dc	6.1	6.198	6.1	6.202	6.1	6.198	90	90	90	90	90	90
B	166	4.884	4.787	4.884	4.788	12.519	12.594	90	90	90	90	120	120
B	58	5.021	4.994	5.585	5.637	6.933	6.647	90	90	90	90	90	90
Ba	bcc	4.996	4.943	4.996	4.943	4.996	4.944	90	90	90	90	90	90
Ba	fcc	6.338	6.355	6.338	6.356	6.338	6.355	90	90	90	90	90	90
Ba	hcp	4.357	4.359	4.357	4.358	14.32	14.324	90	90	90	90	120	120
Ba	dc	7.773	7.924	7.773	7.925	7.773	7.924	90	90	90	90	90	90
Be	hcp	2.241	2.237	2.241	2.237	7.227	7.249	90	90	90	90	120	120
Be	fcc	3.165	3.161	3.165	3.161	3.165	3.161	90	90	90	90	90	90
Be	bcc	2.5	2.506	2.5	2.506	2.5	2.506	90	90	90	90	90	90
Be	dc	4.912	4.912	4.912	4.912	4.912	4.912	90	90	90	90	90	90
Bi	166	4.58	4.53	4.58	4.53	12.067	11.845	90	90	90	90	120	120
Bi	221	3.271	3.222	3.271	3.222	3.271	3.222	90	90	90	90	90	90
Bi	11	4.618	4.56	4.769	4.573	6.472	6.299	87.179	85.9	90	90	90	90
C	194	2.462	2.487	2.462	2.486	6.443	6.443	90	90	90	90	120	120
C	dc	3.554	3.556	3.554	3.556	3.554	3.556	90	90	90	90	90	90
Ca	fcc	5.453	5.402	5.453	5.402	5.453	5.402	90	90	90	90	90	90
Ca	bcc	4.281	4.272	4.281	4.272	4.281	4.272	90	90	90	90	90	90
Ca	dc	8.426	8.372	8.426	8.372	8.426	8.372	90	90	90	90	90	90
Cd	hcp	3.261	3.174	3.261	3.182	9.392	9.71	90	90	90	90	120	120.2
Cd	fcc	4.443	4.379	4.443	4.378	4.443	4.379	90	90	90	90	90	90
Cd	bcc	3.508	3.581	3.508	3.516	3.508	3.378	90	90	90	90	90	90
Cd	dc	6.614	6.766	6.614	6.766	6.614	6.766	90	90	90	90	90	90
Co	hcp	2.441	2.43	2.441	2.43	3.948	3.942	90	90	90	90	120	120
Co	bcc	2.778	2.742	2.778	2.742	2.778	2.742	90	90	90	90	90	90
Co	fcc	3.424	3.42	3.424	3.417	3.424	3.422	90	90	90	90	90	90
Co	dc	5.027	4.842	5.027	5.096	5.027	4.876	90	90	90	90	90	90
Cr	bcc	2.826	2.744	2.826	2.744	2.826	2.744	90	90	90	90	90	90
Cr	fcc	3.58	3.472	3.58	3.472	3.58	3.472	90	90	90	90	90	90
Cr	hcp	2.425	2.434	2.425	2.426	8.835	8.239	90	89.9	90	90	120	119.8
Cr	dc	5.032	4.902	5.032	4.902	5.032	4.902	90	90	90	90	90	90
Cu	fcc	3.612	3.673	3.612	3.668	3.612	3.676	90	90	90	90	90	90
Cu	hcp	2.569	2.61	2.569	2.61	8.251	8.42	90	90	90	90	120	120
Cu	bcc	2.87	2.903	2.87	3.063	2.87	2.902	90	90	90	90.3	90	90.1
Cu	dc	5.328	5.462	5.328	5.462	5.328	5.462	90	90	90	90	90	90

Element	Crystal Structure or Space Group	a [DFT] (Å)	a [HyBOP] (Å)	b [DFT] (Å)	b [HyBOP] (Å)	c [DFT] (Å)	c[HyBOP] (Å)	α [DFT] (degree)	α [HyBOP] (degree)	β [DFT] (degree)	β[HyBOP] (degree)	γ [DFT] (degree)	γ [HyBOP] (degree)
Fe	bcc	2.795	2.792	2.795	2.792	2.795	2.792	90	90	90	90	90	90
Fe	hcp	2.439	2.452	2.439	2.452	7.895	7.994	90	90	90	90	120	120
Fe	fcc	3.428	3.464	3.428	3.459	3.428	3.466	90	90	90	90	90	90
Fe	dc	4.837	4.826	4.837	4.826	4.837	4.826	90	90	90	90	90	90
Ga	64	4.498	4.388	4.498	4.566	4.613	4.442	90	89.6	90	90	119.311	118.3
Ga	63	4.561	4.504	4.561	4.616	4.613	4.572	90	90	90	90	118.229	119.6
Ga	166	7.835	10.833	7.835	8.518	7.835	8.321	72.227	95.7	72.227	70	72.227	78.1
Ge	dc	5.784	5.86	5.784	5.855	5.784	5.86	90	90.2	90	90.2	90	90
Ge	hcp	3.02	3.03	3.02	3.032	9.792	9.89	90	90	90	90.1	120	120
Ge	fcc	4.272	4.257	4.272	4.258	4.272	4.262	90	90.2	90	90.3	90	90.2
Ge	bcc	3.402	3.404	3.402	3.671	3.402	3.125	90	90	90	90.4	90	89.9
Hf	hcp	2.373	2.314	2.373	2.314	7.688	7.47	90	90	90	90	120	120
Hf	fcc	3.348	3.267	3.348	3.266	3.348	3.267	90	90	90	90	90	90
Hf	bcc	2.642	2.607	2.642	2.607	2.642	2.607	90	90	90	90	90	90
Hf	dc	6.438	6.242	6.438	6.243	6.438	6.243	90	90.2	90	90	90	90
In	225	3.383	3.367	3.383	3.367	3.383	3.367	60	60	60	60	60	60
In	139	3.482	3.395	3.482	3.396	3.482	3.414	124.831	122	124.831	122.1	81.817	86.4
In	194	3.347	3.349	3.347	3.349	5.692	5.582	90	90	90	90	120	120
Ir	fcc	3.86	3.86	3.86	3.86	3.86	3.86	90	90	90	90	90	90
Ir	hcp	2.742	2.734	2.742	2.735	8.913	8.914	90	90	90	90	120	120
Ir	bcc	3.102	3.1	3.102	3.101	3.102	3.098	90	90	90	90	90	90
Ir	dc	5.553	5.56	5.553	5.56	5.553	5.56	90	90	90	90	90	90
K	bcc	4.962	4.33	4.962	4.331	4.962	4.33	90	90	90	90	90	90
K	hcp	4.494	4.106	4.494	4.193	7.042	6.48	90	90	90	90	120	122
K	fcc	4.179	3.808	4.179	3.808	4.179	3.807	90	90	90	90	90	90
K	dc	9.12	7.793	9.12	7.793	9.12	7.793	90	90	90	90	90	90
Li	bcc	3.433	3.506	3.433	3.495	3.433	3.658	90	90.1	90	90.3	90	89.6
Li	hcp	3.082	3.145	3.082	3.129	4.94	5.058	90	90	90	90	120	119.6
Li	fcc	4.311	4.457	4.311	4.454	4.311	4.449	90	90.1	90	90	90	90
Li	dc	6.038	5.876	6.038	6.788	6.038	5.908	90	90.1	90	90.2	90	90
Mg	hcp	3.181	3.234	3.181	3.234	5.223	5.306	90	90	90	90.1	120	120
Mg	fcc	4.516	4.607	4.516	4.6	4.516	4.611	90	90.1	90	90.2	90	90.1
Mg	bcc	3.575	3.655	3.575	3.656	3.575	3.652	90	90	90	90	90	90
Mg	dc	6.822	6.669	6.822	6.964	6.822	6.69	90	90.1	90	90.2	90	90
Mo	bcc	3.142	3.042	3.142	3.042	3.142	3.042	90	90	90	90	90	90
Mo	fcc	3.983	3.842	3.983	3.841	3.983	3.842	90	90	90	90	90	90
Mo	hcp	2.693	2.681	2.693	2.675	9.834	9.179	90	90	90	90	120	119.9
Mo	dc	5.632	5.48	5.632	5.48	5.632	5.48	90	90	90	90	90	90
Mn	213	5.987	5.79	5.987	5.79	5.987	5.79	90	90	90	90	90	90
Mn	dc	4.905	4.916	4.905	4.916	4.905	4.916	90	90	90	90	90	90
Na	bcc	4.182	3.897	4.182	3.897	4.182	3.897	90	90	90	90	90	90
Na	fcc	5.28	5.062	5.28	5.062	5.28	5.061	90	90	90	90	90	90
Na	hcp	5.315	4.877	5.315	4.931	6.914	6.48	90	90	90	90	120	121.3
Na	dc	7.449	7.183	7.449	7.183	7.449	7.183	90	90	90	90	90	90
Nb	bcc	3.314	3.19	3.314	3.19	3.314	3.19	90	90	90	90	90	90
Nb	fcc	4.227	4.083	4.227	4.083	4.227	4.083	90	90	90	90	90	90
Nb	hcp	2.811	2.779	2.811	2.786	10.69	10.444	90	90	90	90	120	120.2
Nb	dc	5.93	5.914	5.93	5.914	5.93	5.914	90	90	90	90	90	90
Ni	fcc	3.493	3.484	3.493	3.479	3.493	3.486	90	90.1	90	90.1	90	90
Ni	hcp	2.494	2.48	2.494	2.481	7.922	7.993	90	90	90	90.1	120	120
Ni	bcc	2.786	2.786	2.786	2.786	2.786	2.786	90	90	90	90	90	90
Ni	dc	5.069	4.878	5.069	5.044	5.069	5.227	90	90	90	90.1	90	90

Element	Crystal Structure or Space Group	a [DFT] (Å)	a [HyBOP] (Å)	b [DFT] (Å)	b [HyBOP] (Å)	c [DFT] (Å)	c[HyBOP] (Å)	α [DFT] (degree)	α [HyBOP] (degree)	β [DFT] (degree)	β[HyBOP] (degree)	γ [DFT] (degree)	γ [HyBOP] (degree)
Os	hcp	2.735	2.722	2.735	2.722	8.78	8.817	90	90	90	90	120	120
Os	fcc	3.842	3.836	3.842	3.836	3.842	3.836	90	90	90	90	90	90
Os	bcc	3.081	3.066	3.081	3.066	3.081	3.066	90	90	90	90	90	90
Os	dc	5.53	5.523	5.53	5.776	5.53	5.518	90	90	90	90	90	90
P	2	7.365	7.302	11.921	11.977	12.545	12.456	104.485	104.6	106.151	106.2	98.875	98.6
P	13	9.202	9.224	9.25	9.252	23.366	23.196	74.841	74.5	90	90	90	90
P	53	3.262	3.31	4.743	4.677	7.407	8.458	90	90	90	90	90	90.1
Pb	fcc	3.327	3.233	3.327	3.242	3.327	3.038	90	90	90	89.9	90	90
Pb	hcp	2.378	2.237	2.378	2.244	7.657	7.271	90	90	90	89.7	120	120.2
Pb	bcc	2.66	2.586	2.66	2.587	2.66	2.58	90	90	90	90	90	90
Pb	dc	7.025	7.147	7.025	7.147	7.025	7.147	90	90	90	90	90	90
Pd	fcc	3.917	3.928	3.917	3.926	3.917	3.93	90	90	90	90	90	90
Pd	bcc	3.12	2.959	3.12	3.547	3.12	2.932	90	90	90	90.1	90	89.9
Pd	hcp	2.81	2.794	2.81	2.794	8.846	8.98	90	90	90	90	120	120
Pd	dc	5.745	5.752	5.745	5.752	5.745	5.752	90	90	90	90	90	90
Pt	fcc	3.956	3.97	3.956	3.97	3.956	3.97	90	90	90	90	90	90
Pt	bcc	3.142	3.152	3.142	3.152	3.142	3.152	90	90	90	90	90	90
Pt	hcp	2.88	2.862	2.88	2.866	8.532	8.779	90	90	90	90	120	120.1
Pt	dc	5.746	5.876	5.746	5.926	5.746	5.88	90	90	90	90	90	90
Rb	hcp	5.099	4.548	5.099	4.594	16.192	14.668	90	90	90	90	120	120.9
Rb	fcc	7.144	6.529	7.144	6.529	7.144	6.529	90	90	90	90	90	90
Rb	bcc	5.662	5.264	5.662	5.264	5.662	5.264	90	90	90	90	90	90
Rb	dc	10.348	10.243	10.348	10.243	10.348	10.243	90	90	90	90	90	90
Re	hcp	2.757	2.752	2.757	2.753	8.983	8.978	90	90	90	90	120	120
Re	fcc	3.905	3.896	3.905	3.896	3.905	3.896	90	90	90	90	90	90
Re	bcc	3.107	3.094	3.107	3.094	3.107	3.094	90	90	90	90	90	90
Re	dc	5.622	5.776	5.622	5.776	5.622	5.776	90	90	90	90	90	90
Rh	fcc	3.802	3.755	3.802	3.756	3.802	3.755	90	90	90	90	90	90
Rh	hcp	2.707	2.659	2.707	2.659	8.714	8.749	90	90	90	90	120	120
Rh	bcc	3.05	3.05	3.05	3.05	3.05	3.05	90	90	90	90	90	90
Rh	dc	5.47	5.458	5.47	5.458	5.47	5.458	90	90	90	90	90	90
Ru	hcp	2.706	2.646	2.706	2.647	4.246	4.228	90	90	90	90	120	120
Ru	fcc	3.783	3.72	3.783	3.72	3.783	3.72	90	90	90	90	90	90
Ru	bcc	3.03	2.971	3.03	2.971	3.03	2.971	90	90	90	90	90	90
Ru	dc	5.402	5.532	5.402	5.532	5.402	5.532	90	90	90	90	90	90
S	148	6.387	6.238	6.387	6.462	6.387	6.316	113.668	112.9	113.668	115.8	113.668	113.7
Sb	166	4.37	4.382	4.37	4.377	11.588	11.715	90	90	90	90	120	120
Sb	221	3.104	3.142	3.104	3.196	3.104	3.14	90	90	90	90	90	90.1
Sb	11	4.362	4.452	3.161	3.128	4.359	4.329	88.936	89.9	90	89.9	90	88.4
Sc	hcp	3.273	3.303	3.273	3.3	5.175	5.299	90	90	90	90	120	119.8
Sc	fcc	4.586	4.631	4.586	4.631	4.586	4.632	90	90	90	90	90	90
Sc	bcc	3.653	3.605	3.653	3.605	3.653	3.605	90	90	90	90	90	90
Sc	dc	6.402	7.281	6.402	7.281	6.402	7.281	90	90	90	90	90	90
Se	152	4.349	4.153	4.349	4.18	5.075	5.324	90	91.8	90	87.8	120	120.8
Se	148	6.57	7.322	6.57	7.053	6.57	7.006	113.509	130.1	113.509	98.6	113.509	114.2
Si	dc	5.465	5.531	5.465	5.53	5.465	5.53	90	90	90	90	90	90
Si	hcp	2.712	2.721	2.712	2.722	9.047	9.006	90	90	90	90.2	120	120
Si	bcc	3.075	3.243	3.075	2.986	3.075	2.902	90	90	90	90.1	90	90.1
Si	fcc	3.863	3.831	3.863	3.828	3.863	3.833	90	90.1	90	90.2	90	90
Sn	139	3.309	3.359	3.309	3.359	3.309	3.357	105.538	105.8	105.538	105.6	117.661	117.4

Element	Crystal Structure or Space Group	a [DFT] (Å)	a [HyBOP] (Å)	b [DFT] (Å)	b [HyBOP] (Å)	c [DFT] (Å)	c[HyBOP] (Å)	α [DFT] (degree)	α [HyBOP] (degree)	β [DFT] (degree)	β[HyBOP] (degree)	γ [DFT] (degree)	γ [HyBOP] (degree)
Sr	fcc	4.485	4.384	4.485	4.384	4.485	4.38	90	90	90	90	90	90
Sr	bcc	3.538	3.499	3.538	3.499	3.538	3.499	90	90	90	90	90	90
Sr	hcp	3.196	3.11	3.196	3.11	10.291	10.109	90	90	90	90	120	120
Sr	dc	9.463	9.302	9.463	9.302	9.463	9.302	90	90	90	90	90	90
Ta	bcc	3.304	3.3	3.304	3.3	3.304	3.299	90	90	90	90.1	90	90
Ta	fcc	4.2	4.201	4.2	4.196	4.2	4.206	90	90.2	90	90.2	90	90.1
Ta	hcp	2.816	2.924	2.816	2.913	10.391	9.932	90	90	90	90.1	120	119.8
Ta	dc	6.052	6.079	6.052	6.079	6.052	6.079	90	90	90	90	90	90
Te	152	4.481	4.463	4.481	4.464	5.971	5.963	90	90	90	90	120	120
Te	51	3.159	3.122	4.647	4.502	8.893	8.816	90	90	90	90	90	90
Te	26	3.173	3.129	4.63	4.494	8.891	8.815	90	90	90	90	90	90
Te	12	4.452	4.392	4.452	4.398	5.744	5.612	89.521	89.8	89.521	89.7	60.119	60
Te	221	3.196	3.141	3.196	3.141	3.196	3.141	90	90	90	90	90	90
Te	166	3.196	3.141	3.196	3.141	3.196	3.141	88.646	89	88.646	89	88.646	89
Ti	hcp	2.902	2.91	2.902	2.91	9.366	9.446	90	90	90	90	120	120
Ti	fcc	4.082	4.105	4.082	4.105	4.082	4.105	90	90	90	90	90	90
Ti	bcc	3.229	3.238	3.229	3.238	3.229	3.238	90	90	90	90	90	90
Ti	dc	5.894	6.289	5.894	6.289	5.894	6.289	90	90.1	90	90.1	90	90.1
Tl	hcp	3.608	3.346	3.608	3.37	5.49	5.299	90	90	90	90	120	120.6
Tl	bcc	3.961	3.914	3.961	3.914	3.961	3.914	90	90	90	90	90	90
Tl	fcc	5.002	4.954	5.002	4.955	5.002	4.954	90	90	90	90	90	90
Tl	dc	7.034	7.109	7.034	7.111	7.034	7.108	90	89.9	90	89.8	90	90
V	bcc	2.969	2.956	2.969	2.961	2.969	2.952	90	90	90	89.8	90	89.8
V	fcc	3.768	3.76	3.768	3.8	3.768	3.754	90	89.8	90	89.6	90	89.8
V	hcp	2.496	2.54	2.496	2.532	9.523	9.285	90	90	90	90	120	119.6
V	dc	5.388	5.269	5.388	5.269	5.388	5.269	90	90	90	90	90	90
W	bcc	3.165	3.218	3.165	3.198	3.165	3.217	90	90	90	90.2	90	90.1
W	fcc	4.011	4.003	4.011	4	4.011	4.01	90	90.2	90	90.4	90	90.2
W	hcp	2.743	2.874	2.743	2.876	9.787	9.712	90	89.9	90	90.2	120	120
W	dc	5.788	5.664	5.788	5.838	5.788	5.611	90	90.2	90	90.4	90	90.2
Y	hcp	3.57	3.449	3.57	3.449	5.727	5.582	90	90	90	90	120	120
Y	fcc	5.038	4.871	5.038	4.874	5.038	4.872	90	90	90	90	90	90
Y	bcc	4.032	3.931	4.032	3.931	4.032	3.931	90	90	90	90	90	90
Y	dc	7.061	6.444	7.061	6.444	7.061	6.444	90	90	90	90	90	90
Zn	hcp	2.627	2.677	2.627	2.669	5.251	4.891	90	90	90	90	120	119.7
Zn	fcc	3.899	3.931	3.899	3.927	3.899	3.934	90	90.2	90	90.2	90	90.2
Zn	bcc	3.089	3.089	3.089	3.088	3.089	3.087	90	90	90	90.1	90	90
Zn	dc	5.779	5.623	5.779	5.907	5.779	6.54	90	90.1	90	90.1	90	90.1
Zr	hcp	3.215	3.223	3.215	3.223	5.147	5.212	90	90	90	90	120	120
Zr	fcc	4.477	4.523	4.477	4.523	4.477	4.523	90	90	90	90	90	90
Zr	bcc	3.531	3.524	3.531	3.524	3.531	3.524	90	90	90	90	90	90
Zr	dc	6.235	6.67	6.235	6.86	6.235	6.864	90	90.6	90	90.4	90	90.2

Extended Table 5: The stiffness modulus ($C_{11}, C_{22}, C_{33}, C_{44}, C_{12}$ and C_{13} for the considered 54 elements, as predicted by the c-MCTS optimized Hybrid Bond Order potentials. The relevant structures in each case were collected from the Materials Project database [46].

Element	Crystal Structure or Space Group	C_{11} [DFT] (GPA)	C_{11} [HyBOP] (GPA)	C_{22} [DFT] (GPA)	C_{22} [HyBOP] (GPA)	C_{33} [DFT] (GPA)	C_{33} [HyBOP] (GPA)	C_{44} [DFT] (GPA)	C_{44} [HyBOP] (GPA)	C_{12} [DFT] (GPA)	C_{12} [HyBOP] (GPA)	C_{13} [DFT] (GPA)	C_{13} [HyBOP] (GPA)
Ag	fcc	100	124.4	100	120.4	100	123.5	41	38.2	82	102	82	103.2
Al	fcc	104	122	104	121.9	104	121.6	32	47.3	73	94	73	93.6
As	166	127	64	127	64	30	82.8	32	24	40	39.9	25	58.7
Au	fcc	144	142.4	144	142.4	144	142.3	29	62	134	107.1	134	107.2
B	166	453	381.4	453	379.5	602	395.9	208	35.3	113	265.6	43	309.5
Ba	bcc	12	9.8	12	9.7	12	9.7	10	17.4	7	5.9	7	5.9
Be	hcp	322	620.5	322	620.5	378	728.4	162	147	21	328	8	205.8
Bi	166	68	42.9	68	46.4	30	53.0	10	2.6	24	36.9	19	36.3
C	194	904	991.1	904	992.2	8	0	2	0	159	422.8	-1	-0.2
Ca	fcc	21	31.2	21	31.2	21	31.2	14	22.6	15	19.3	15	19.3
Cd	hcp	87	103.6	87	100.7	43	121.2	11	27.9	39	40.5	28	30.9
Co	hcp	358	279	358	273.8	409	367	95	58.7	165	174.6	114	103.5
Cr	bcc	499	300	499	253	499	326	102	91.4	139	193.5	139	137.5
Cu	fcc	180	144.1	180	140.3	180	142.4	78	108.3	127	130.6	127	127
Fe	bcc	247	265.4	247	190.4	247	261.2	97	85	150	165	150	92.8
Ga	64	91	46	116	43.6	84	45.3	29	33.8	22	33.1	31	30
Ge	dc	104	61.6	104	59.2	104	61.7	56	5.9	37	53.3	37	53.8
Hf	hcp	184	329.1	184	328	194	253.9	52	73.6	70	234.9	68	69.2
In	225	42	72.4	42	72.2	43	75.8	6	14.6	23	35.1	33	31.1
Ir	fcc	576	247.6	576	247.3	576	245.6	252	179.4	231	231.4	231	226.7
K	bcc	3	13.6	3	13	3	14.2	3	9.2	4	2.6	4	4.4
Li	bcc	15	13.6	15	26.4	15	16.1	11	24.2	13	16.8	13	12.2
Mg	hcp	58	60	58	55.2	66	68.5	20	12.2	30	34.1	22	7.9
Mo	bcc	472	270.5	472	207.5	472	269	106	111.1	158	167	158	97.5
Mn	213	349	348.1	350	348.1	350	348.1	99	141.8	221	122.8	221	122.8
Na	bcc	9	20.3	9	20.4	9	20.4	7	14.9	7	11.5	7	11.5
Nb	bcc	233	238.1	233	237.9	233	237.8	11	169.3	145	226.9	145	226.9
Ni	fcc	276	283	276	279.4	276	272.8	132	128.6	159	224.4	159	211.3
Os	hcp	730	498.2	730	498.6	824	528.7	252	93.1	226	233.1	220	193.5
P	64	43	579.2	13	34	177	-1870.6	4	116.2	-3	-1098.4	32	1388.3
Pb	fcc	47	59.3	47	70.8	47	106.9	18	37.6	32	22.4	32	50.9
Pd	fcc	187	151	187	148.9	187	144.6	71	71.2	147	106	147	100.1
Pt	fcc	303	276	303	277	303	274.4	54	138	220	183.1	220	181
Rb	hcp	4	14.9	4	14.9	5	14.1	1	3.7	2	7.1	2	4.3
Re	hcp	607	633.6	607	633.6	670	689.3	156	126.6	273	267.5	214	211.1
Rh	fcc	397	233.3	397	228.1	397	232.8	177	100.7	182	183.4	182	186
Ru	hcp	559	784.9	559	784.9	635	945.8	181	214.8	178	336.6	166	262.6
S	148	4	4.6	4	6.7	2	4	1	1.6	0	2.4	1	1.9
Sb	166	91	68.4	91	67.3	38	36.4	27	17.7	24	20.2	21	25.7
Sc	hcp	98	61.8	98	61.8	89	75.4	28	34.3	34	-14	30	-27.8
Se	152	7	31.0	7	28.8	69	36.6	11	7.9	2	14.4	8	19.7
Si	dc	144	109.7	144	109.7	144	109.8	75	13.4	53	90.4	53	90.4
Sn	227	59	64.8	59	65.7	59	12.4	26	2.3	28	43	28	27.8
Ta	bcc	265	270.2	265	269.2	265	261.7	69	179.4	158	284.5	158	281.8
Te	152	30	22.9	30	22.6	66	18.8	29	9.3	7	3.3	21	4.4
Ti	hcp	177	343.7	177	343.3	191	408.2	42	77.4	83	153.8	76	92.7
Tl	hcp	32	46.5	32	54.7	48	89	7	11.2	21	50.1	22	20.6
V	bcc	276	147.6	276	117	276	151.7	16	17.2	131	130.7	131	117.9
W	bcc	510	286.2	510	364.4	510	360.8	143	53.4	201	216.1	201	213.4
Y	hcp	77	58.5	77	58.5	81	78.9	25	4	26	19.6	21	3.8
Zn	hcp	163	151.8	163	148.6	61	96.7	32	18.4	45	66.9	48	18.5
Zr	hcp	144	165.8	144	165.7	162	184.3	26	43.8	65	67.4	67	48.7

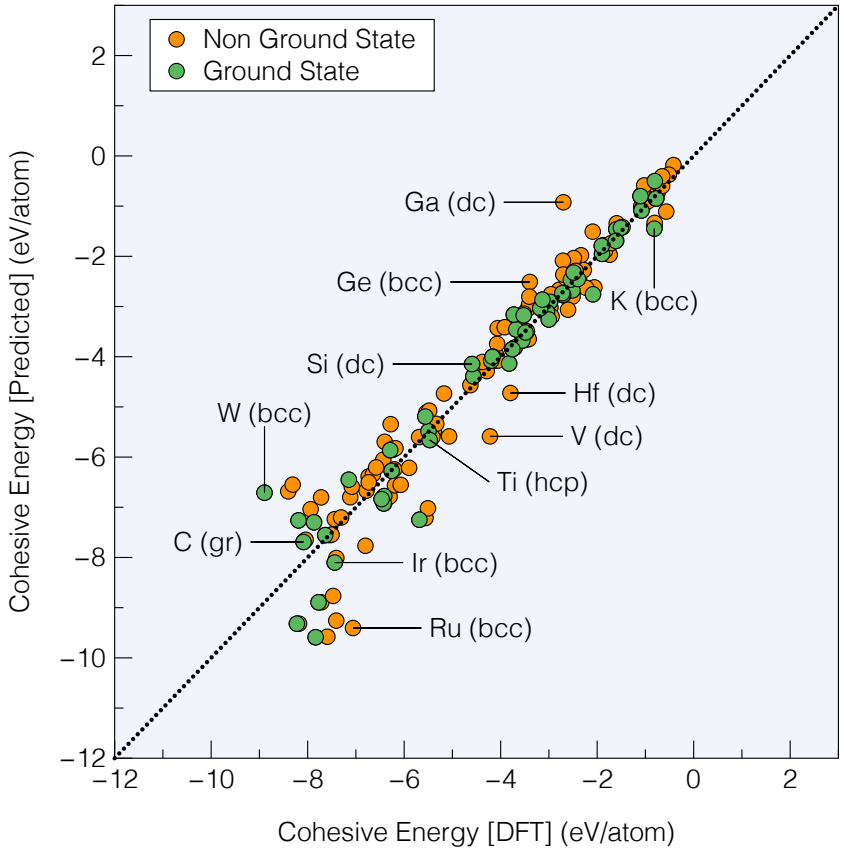

Extended Figure 3: Accuracy of predicted cohesive energies of the different polymorphs (including the ground state) of 54 elements from c-MCTS optimized Hybrid BOP potentials in this study.

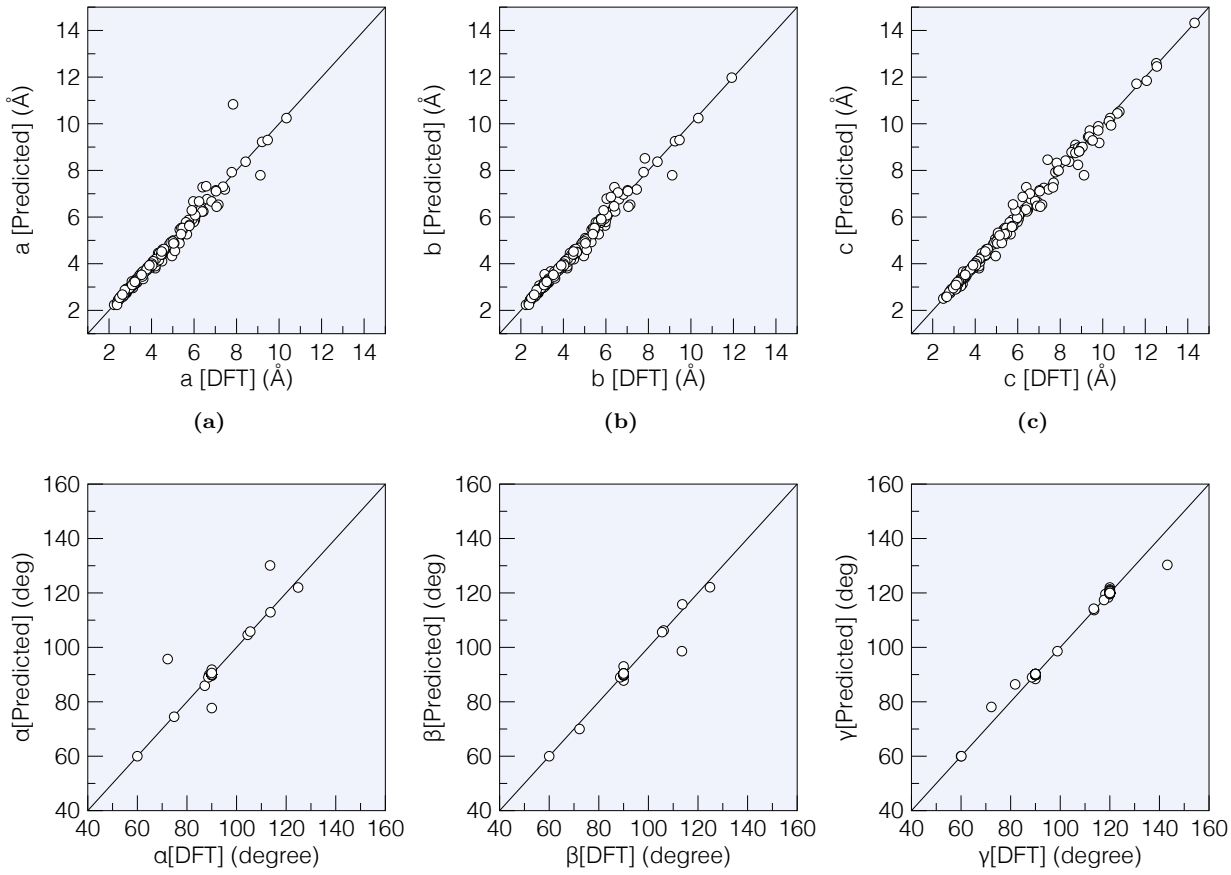

Extended Figure 4: Accuracy of predicted lattice parameters of the different polymorphs (including the ground state) of 54 elements from c-MCTS optimized Hybrid BOP potentials in this study.

Figures

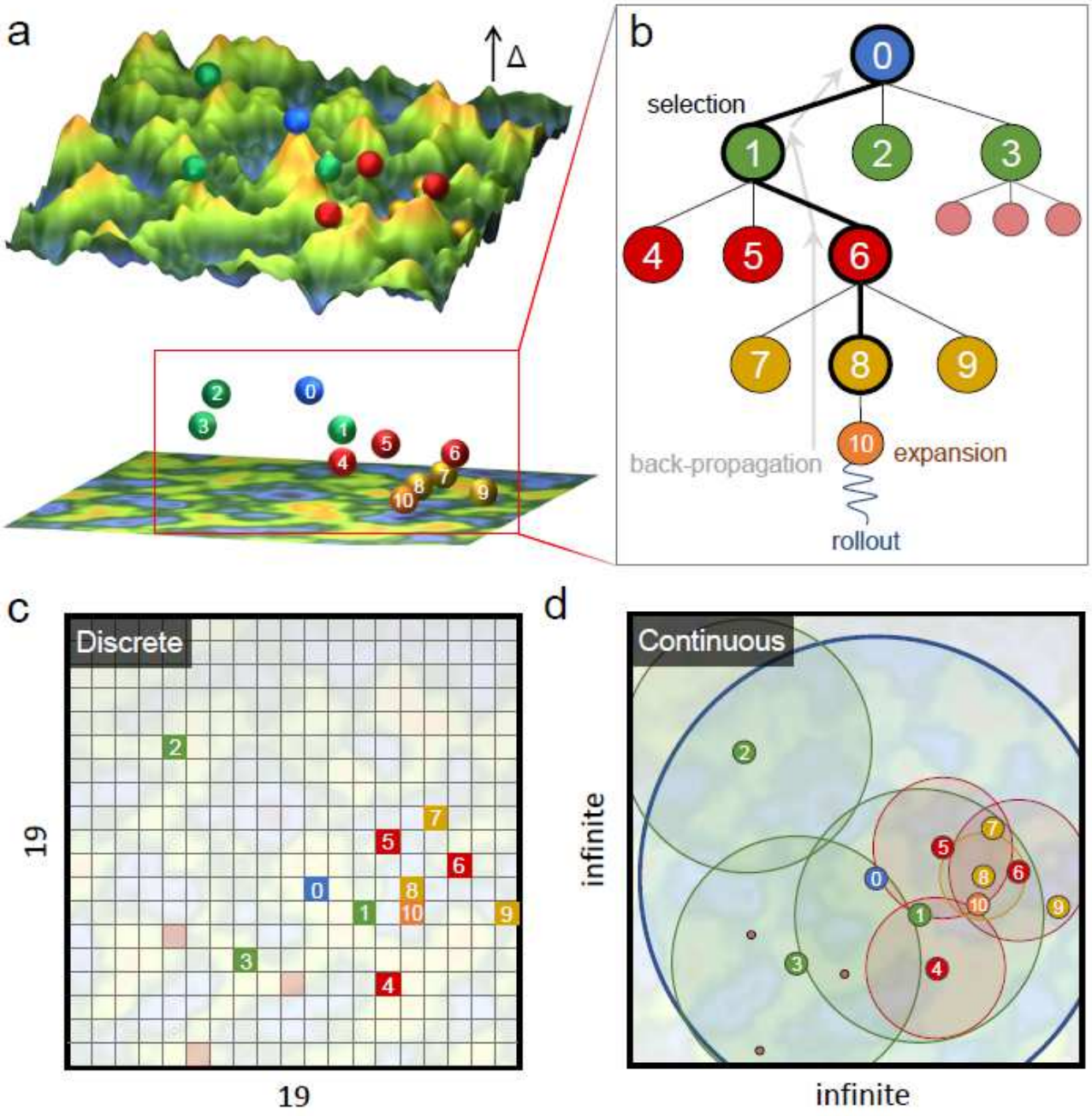

Figure 1

Schematic of the continuous action MCTS algorithm applied for exploration of high- dimensional potential energy surfaces a) Top: Simplistic representation of an objective landscape for a 2-parameter search problem. In-plane axes corresponds to (two) independent model parameters. Outof- plane axis corresponds to objective values, which is dened as the weighted sum of the error in model predicted energies of clusters with respect to target energies. This objective is minimized by our c-MCTS algorithm. The spheres represent candidates of di erent model parameters within a MCTS run, where di erences in

their vertical positions indicate di erences in their objective values. Bottom: Slightly tilted view of the above with the surface represented as a contour map below the spheres. The numbering on the spheres corresponds to their node positions in the MCTS tree shown in (b). These numbers roughly correspond to the order that the candidates are explored. b) Schematic showing the root, parent, child nodes and their relationship within a MCTS tree structure. A typical MCTS search involves node selection, expansion, simulation (playout), and back-propagation. Different coloring of the nodes indicates different depth in the MCTS tree. The algorithm balances between exploration (lateral expansion of nodes) and exploitation (depth expansion of nodes). As shown in (a), the objective value of a MCTS run is expected to decrease quickly along the depth of the tree. c) Search space of a traditional MCTS algorithm, e.g., game board, is discrete. In the context of parameter optimization, for two discrete parameters each of 19 possible values, the search space consists of a nite 361 search positions. d) The problem of parameter search, such as the objective surface illustrated in (a), generally involves parameters that are continuous, which corresponds to innite possible search positions. We handle this challenge by applying a range-funneling technique to the MCTS algorithm where the search neighborhood at each tree depth becomes smaller and smaller such that the algorithm can converges to the optimal solutions.

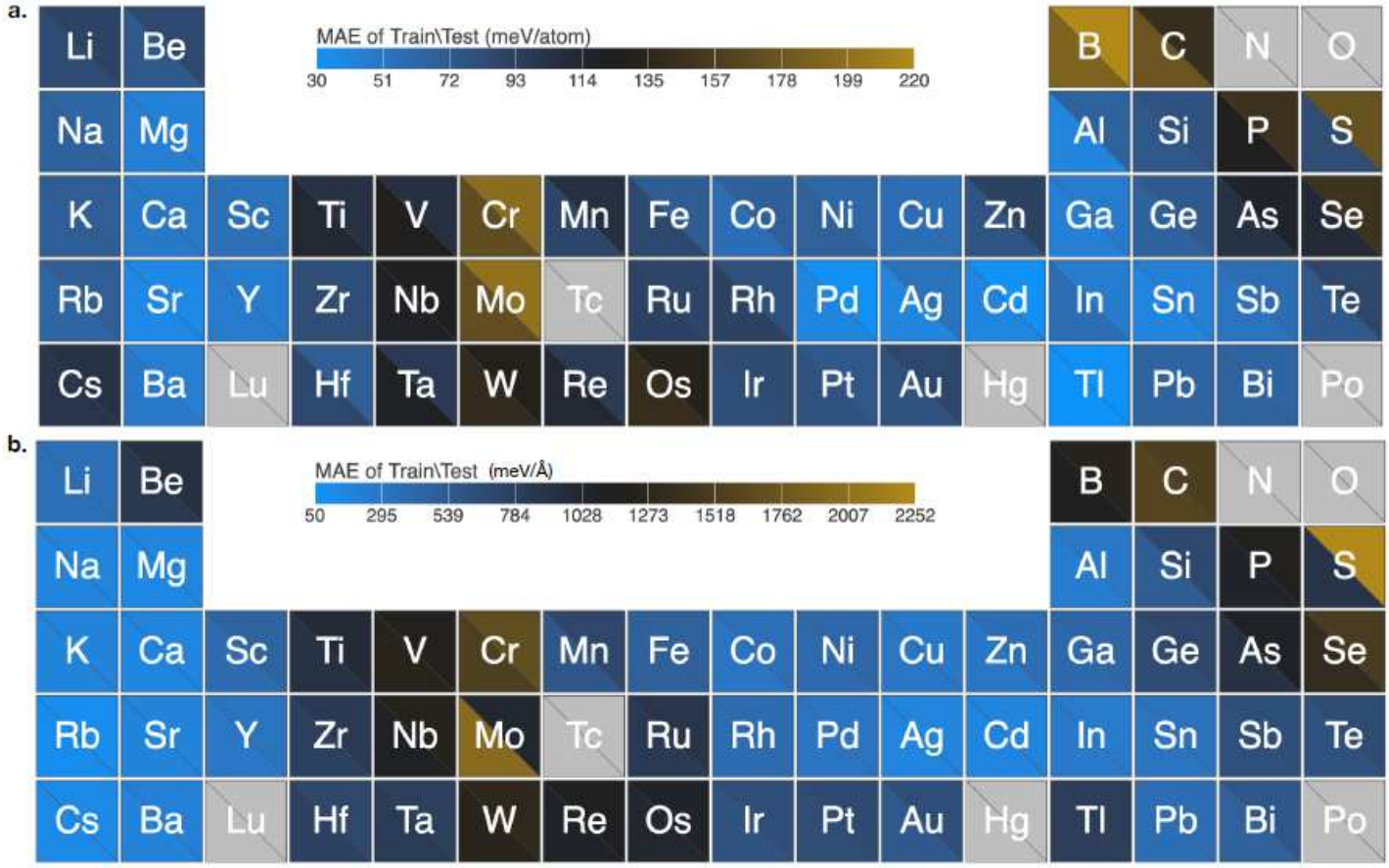

Figure 2

HyBOP model performance after high-throughput exploration of the potential en- ergy surface of nanoclusters using continuous action MCTS. A bond order model with Tersoff-type formalism for 54

different elements across the Periodic table is parameterized using an extensive training dataset generated from density functional theory (DFT) computations. The training set includes nanoclusters of varying sizes and shapes (≈1500 congurations and their energies) for each of the different elements. Mean absolute error (MAE) in (a) energy and (b) force predictions of the bond order force-elds relative to the reference DFT model on a test set of ≈70,000 congurations is shown using the color bar in meV/atom and meV/Å units, respectively.

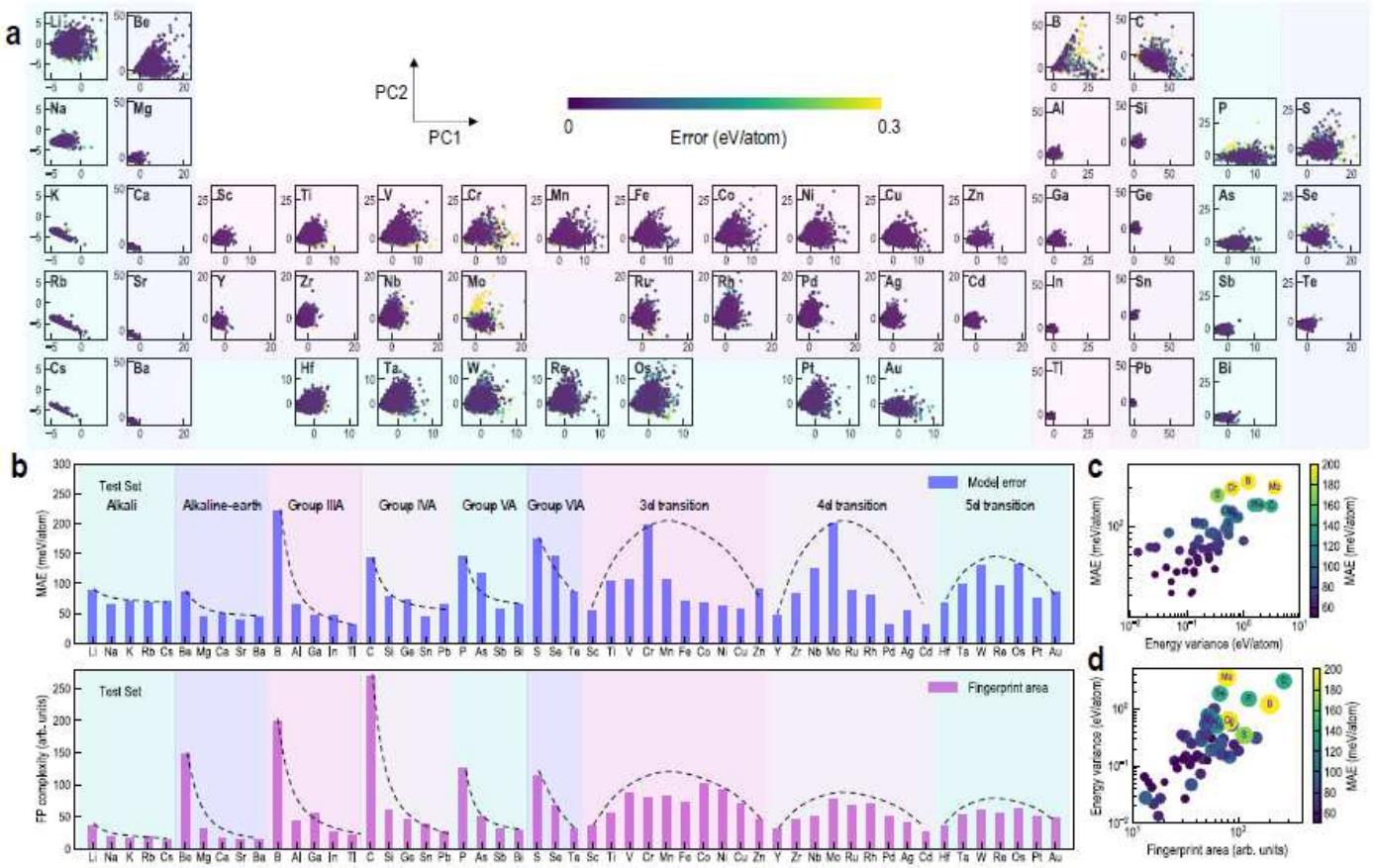

Figure 3

Trends in model prediction errors with structural diversity of the element. (a) SOAP ngerprint representation of clusters across different elements as projected along the rst two principal components (PCs). The area covered by an element in the PC space is proportional to its structural diversity, and thus, the difficulty to train an accurate potential model. Also, the structural diversity of an element is closely related to its position in the Periodic table. Regions of higher errors mostly occur at the boundary of the PC space which are expected to belong to under-represented congurations. (b) Trend in the prediction errors for different elements when grouped across different columns or rows of the Periodic Table. A similar trend can be seen for the elemental PC area, suggesting that elemental structural diversity correlates well with the model errors. The dotted lines capture the approximate trend within a group of elements and guide the eye. (c) Correlation between the prediction error and the inverse of the smoothness of the element energy surface. (d) Elements with high prediction errors display either high

structural diversity or exhibit highly corrugated energy surface. Elements with mean absolute error (MAE) >100 meV/atom have been marked in (c) and (d).

Figure 4

Dynamic stability of the clusters of various representative elemental systems. Snapshots sampled from 1 nanosecond MD simulation trajectories illustrate the dynamic stability of the clusters of representative topologies and sizes for the different elements. To rigorously test the dynamic stability, MD simulations were performed for > 40,000 nanoclusters for the 54 different elements in different size ranges. More detailed MD trajectories for each element and the simulated temperatures are included in the Supplemental Information Section 10.

Supplementary Files

This is a list of supplementary files associated with this preprint. Click to download.

- MCTSOpenAIGymVideos.zip
- supportinginformation.pdf